Geophysical Journal International

Geophys. J. Int. (2016) **206,** 85–102
Advance Access publication 2016 April 6
GJI Seismology

doi: 10.1093/gji/ggw131

Application of a characteristic periods-based (CPB) approach to estimate earthquake-induced displacements of landslides through dynamic numerical modelling

S. Martino,[1] L. Lenti,[2] J. Delgado,[3] J. Garrido[4] and C. Lopez-Casado[5]

[1] *"La Sapienza" University of Rome, Dipartimento di Scienze della Terra and Centro di Ricerca Previsione, Prevenzione e Controllo dei Rischi Geologici (CERI) – Ple A. Moro 5, I-*00185 *Roma, Italy. E-mail: salvatore.martino@uniroma1.it*
[2] *Université Paris-Est, Institute of Science and Technology for Transport, Development and Networks (IFSTTAR),* 14–20 *Boulevard Newton Cité Descartes, Champs sur Marne F-*77447 *Marne la Vallée, France*
[3] *Dpt. Ciencias de la Tierra y del Medio Ambiente, Universidad de Alicante, Ap. Correos* 99*, E-*03080 *Alicante, Spain*
[4] *Dpt. Ingeniería Civil, Universidad de Granada, Campus Fuentenueva, Av. Severo Ochoa s/n. E-*18071 *Granada, Spain*
[5] *Dpt. Física Teórica y del Cosmos, Universidad de Granada, Campus Fuentenueva, Av. Severo Ochoa s/n, E-*18071 *Granada, Spain*

Accepted 2016 April 4. Received 2016 April 4; in original form 2015 October 10

SUMMARY

The interaction between seismic waves and slopes is an important topic to provide reliable scenarios for earthquake-(re)triggered landslides. The physical properties of seismic waves as well as slope topography and geology can significantly modify the local seismic response, influencing landslide triggering. A novel approach is here applied to two case studies in Andalusia (southern Spain) for computing the expected earthquake-induced displacements of existing landslide masses. Towards this aim, dynamic stress–strain numerical modelling was carried out using a selection of seismic signals characterized by different spectral content and energy. *In situ* geophysical measurements, consisting of noise records and temporary seismometric arrays, were carried out to control the numerical outputs in terms of local seismic response. The results consist of relationships between the characteristic period, T_m, of the seismic signals and the characteristic periods of the landslide masses, related to the thickness (T_s) and length (T_l), respectively. These relationships show that the larger the horizontal dimension (i.e. length of landslide) of a landslide is, the more effective the contribution (to the resulting coseismic displacement) of the long-period seismic waves is, as the maximum displacements are expected for a low T_m at each energy level of the input. On the other hand, when the local seismic response mainly depends on stratigraphy (i.e. landslide thickness), the maximum expected displacements occur close to the resonance period of the landslide, except for high-energy seismic inputs.

Key words: Geomorphology; Site effects; Europe.

INTRODUCTION

Possible interactions between seismic waves and slopes for predicting the earthquake-induced movements of landslides have been analysed in several studies (Del Gaudio & Wasowsky 2007; Bourdeau & Havenith 2008; Danneels *et al.* 2008; Lenti & Martino 2012, 2013) to describe how the triggering conditions depend on seismic input properties such as energy, frequency content, directivity and peak ground acceleration (PGA) as well as on the slope topography and geological setting. Some case studies (Bozzano *et al.* 2008, 2011; Alfaro *et al.* 2012; Delgado *et al.* 2015; Martino 2015) highlighted the role of these interactions in response to seismic amplification effects. More in particular, it was already highlighted (Delgado *et al.* 2011) that pre-existing large landslides can represent outliers with respect to the predictive curves proposed by Keefer (1984) and Rodriguez *et al.* (1999), as they can interact with far-field earthquakes characterized by long-period spectral content.

Earthquake-reactivated landslides more commonly involve cohesive soils or debris; generally, it is possible to inventory these landslides as active or quiescent phenomena that can be recognized by typical landforms or historical chronicles that document their past (re)activations. Although these events are directly recognizable, a great effort is needed to evaluate how their stability conditions change due to earthquake occurrence as well as to quantify their coseismic or post-seismic mobility in terms of their expected displacements. This difficulty depends on the complex interactions between the seismic waves and the existing landslide mass, which is conditioned by several features, among which are the slope geometry, landslide mass properties and physical characteristics of the seismic waves.

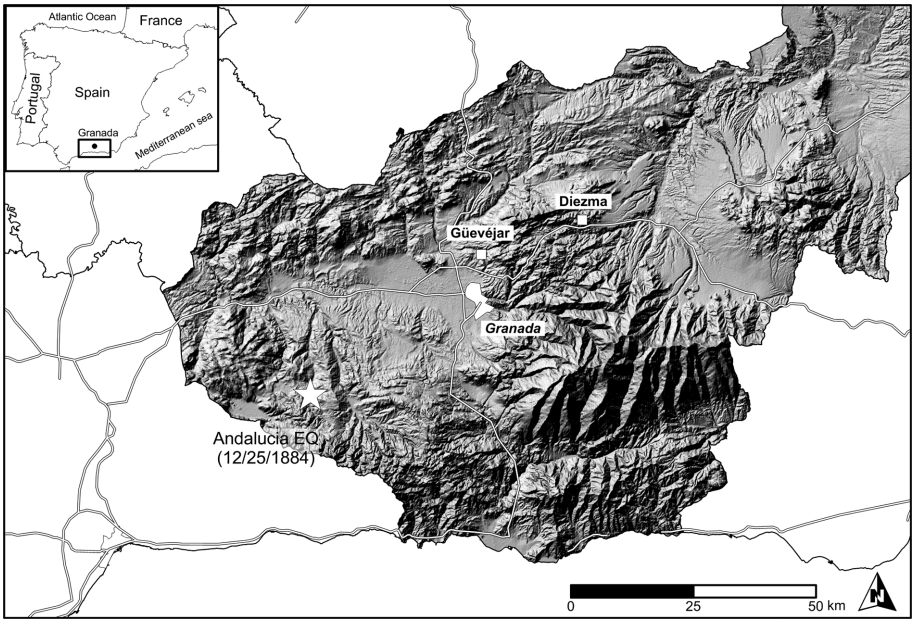

Figure 1. Locations of the Güevejar and Diezma landslide in the Andalusia region (Southern Spain).

According to the more traditional rigid or flexible sliding block methods (Newmark 1965; Makdisi & Seed 1978; Rathje & Bray 2000), the maximum expected earthquake-induced displacements correspond to a resonant period due to the landslide mass thickness (T_s) equal to the characteristic period (T_m) of the seismic input (Rathje *et al.* 1998), which depends on the frequency content expressed by the fast Fourier transform (FFT). A characteristic period ratio T_s/T_m was introduced to describe such conditions, that is a maximum displacement is theoretically expected for a T_s/T_m ratio equal to 1. Stress–strain numerical models by finite element method (FEM) and finite difference method (FDM) codes can be focused on evaluating the landslide mass stability under seismic action and predicting both the coseismic and post-seismic earthquake-induced displacements. These analyses allow assuming that deformations can occur within the landslide mass and simulating more complex interactions between seismic waves and the slope by considering 2-D geometric configurations.

Recent studies have also focused on the effects of step-like slope geometries on the local seismic response (Bouckovalas & Papadimitriou 2005; Lenti & Martino 2012, 2013). The results of these studies demonstrate that the differences among the displacements computed by Newmark's approach and those computed by dynamic stress–strain numerical models are not negligible. In particular, the higher the slope angle is, the greater are the resulting differences for the same seismic input and for the same mechanical properties of the landslide mass from those computed by dynamic stress–strain numerical models. According to these results, the role of the 2-D geometry (i.e. slope angle and landslide mass length) cannot be neglected for a better prediction of earthquake-induced landslide displacements. In particular, the landslide mass mobility is theoretically favoured (Hutchinson 1994) by the characteristic period of the seismic input (T_m), which is double with respect to the period (T_l) associated with the length of the landslide mass itself (i.e. for a characteristic period ratio T_l/T_m equal to 0.5). According to this characteristic periods-based (CPB) approach, the values of the expected earthquake-induced landslide displacements depend on a combination of 1-D and 2-D effects, these last ones related to the more complex interactions between the landslide mass and slope geometry. Numerical results (Lenti & Martino 2013) have demonstrated that upon increasing the energy of the input, the 2-D effects become more significant, and the expected displacements are mainly related to the T_l/T_m ratio. On the other hand, the 1-D resonance of the landslide mass is much more evident in the case of more gentle slopes than for steeper ones.

In this study, the CPB approach was applied to provide the expected displacements of the Güevejar and Diezma landslides located in Andalusia (Southern Spain; Fig. 1). Although they have similar geographical locations, the two landslides are characterized by different dimensions, slope geometries and local geological settings.

The Güevejar landslide was historically reactivated (Jiménez Pintor & Azor 2006) by the 1755 Lisbon earthquake (M_w 8.5), with an epicentral distance greater than 500 km and by the 1884 Andalusia earthquake (M_w 6.5), with an epicentral distance greater than 50 km (Fig. 1), although it was not re-activated by the numerous $M_w > 5.0$ local earthquakes with epicentral distances lower than 50 km that occurred during the same time interval (Rodriguez-Peces *et al.* 2011). Historical sources report that after the 1755 landslide reactivation (Sanz 1997), up to 2 m opened cracks were observed; as a consequence of the earthquake-induced landslide movement, the old Güevejar village was moved to its actual location, that is SW from the landslide area (Figs 2a and b).

The Diezma landslide, man-induced by the construction of the A-92 Highway in 1991 (Fig. 2c), was triggered the first time by rainfalls but it was not triggered by earthquakes so far, although several reactivations are known prior to 2011 (Delgado *et al.* 2015; Fig. 2d). Due to the state of activity of the landslide, earthquakes may further destabilize its mass and must be taken into account. The Diezma landslide is located in a region of moderate seismicity with a maximum PGA of approximately 0.16 g, for an expected return period of 475 yr (Martínez-Solares *et al.* 2013). However, no strong earthquakes (M_w greater than 5.0) have occurred within 50 km of the site since the generalized slope failure in 2001.

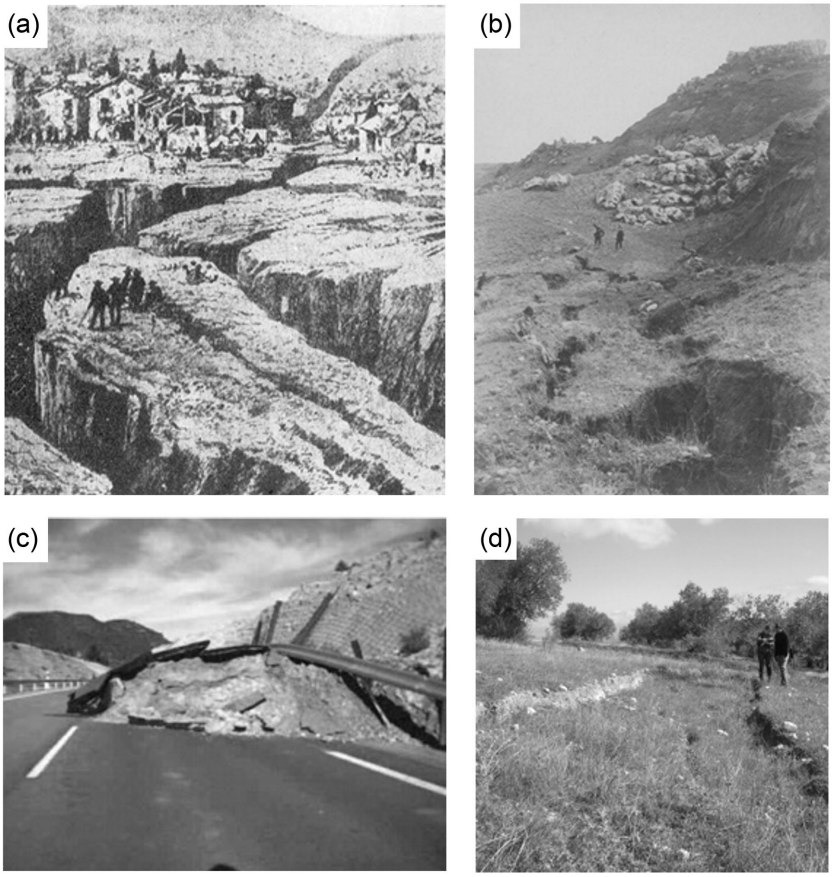

Figure 2. Reactivation of the Güevejar landslide during the 1884 Andalusia earthquake as documented by a painting of an unknown author (a) (painting from Meléndez & Fuster 1966) and by a picture recovered at the French National Library (b). Diezma landslide failure occurred during the construction of the A-92 highway, (c) and the reactivation of the landslide occurred in 2013 (d).

CASE STUDIES

Güevejar landslide

The Güevejar landslide is located 10 km N of the city of Granada; it is approximately 1500 m in length and 540 m in width and covers an area of approximately 56 ha (Fig. 3). The elevation difference between the crown area and the landslide tip is approximately 130 m, and the average inclination of the slope is 13°; the sliding surface has an average depth of 50 m, and the estimated volume is approximately 30 Mm^3. The landslide is characterized by a complex mechanism (Cruden & Varnes 1996) consisting of a roto-translational sliding passing downhill to an earthflow that reaches the bottom of the valley, where it is eroded by the Bermejo river. Currently, the landslide is dormant (sensu WP/WLI 1993), but it has well-preserved landforms, including a main scarp and three orders of counterslope terraces separated by secondary scarps, showing that it was active in the recent past. It involves Miocene to Pleistocene deposits that fill the Granada basin (IGME 1988); more in particular, the stratigraphy of the site is characterized by a Neogene-Quaternary succession of marine deposits passing to continental ones. From bottom to top, these deposits include grey clays with silty and sandy levels (Upper Miocene), grey clays with gypsum levels (Upper Miocene), grey marls with lignite (Upper Miocene), red silts (Upper Miocene), lacustrine limestones and marls (Upper Miocene) and red silts with sandstone and conglomerate levels (Pliocene–Pleistocene). The landslide mass mainly contains Upper Miocene red silts and partially, corresponding to the crown area, lacustrine limestones and marls of the Upper Miocene.

The geological cross-section (Fig. 4a), reconstructed along the Güevejar landslide mass using field survey evidence as well as 2 borehole stratigraphic logs, shows a monoclinal NW dipping assessment of the Upper Miocene deposits. A fault line causes the marls with lignite to outcrop along the slope SE of the hill top.

The engineering-geological model of the landslide (Fig. 4a, Table 1) was built by considering seismo-stratigraphies derived from 2 downhole tests specifically performed in drilled boreholes; data from *f–k* arrays, refraction microtremor tests (ReMi) and multichannel analysis of surface waves (MASW) are available in technical reports possessed by the Junta de Andalusia administration. These investigations are shown in Fig. 3, while Fig. 5 reports the seismo-stratigraphies corresponding to the S1 and S2 boreholes, which result from the down-hole tests, and the seismo-stratigraphies obtained from ReMi R7 and array *f–k* A5 are located along the section of Fig. 4. On the basis of the engineering-geological data and considering the distribution of shear wave velocity (*Vs*), the landslide mass can be divided into three portions (upper, middle and lower), distinguished in terms of *Vs* that range from 335 up to 700 m s^{-1}. In particular, the middle portion of the landslide mass is characterized by the highest *Vs* values. The seismic bedrock is encountered immediately below the landslide mass as the measured *Vs* exceeds 750 m s^{-1}, except for the lower portion of the hill slope where the earthflow is located.

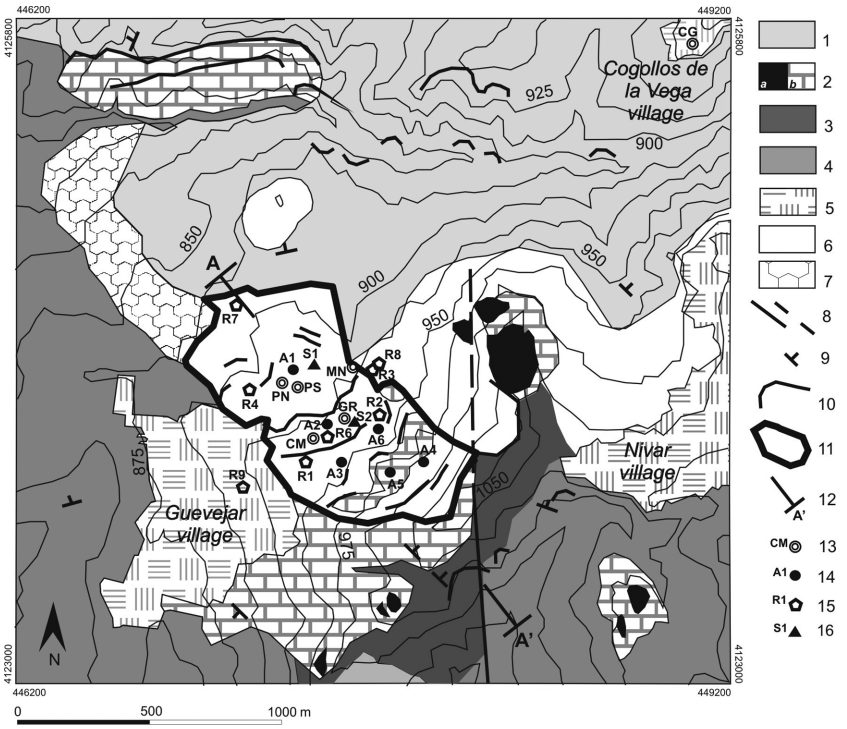

Figure 3. Geological map of the Güevejar landslide area (geographic coordinates are provided in UTM-ED50 reference system): (1) red silts, sands and conglomerates (Plio-Pleistocene), (2) Lacustrine limestones (a) and marls (b) (upper Miocene), (3) red silts with cemented conglomerates (upper Miocene), (4) grey clays with gypsum, silts and marls with lignite (upper Miocene), (5) urbanized areas, (6) slope debris, (7) earthflow, (8) fault (dashed if supposed), (9) attitude of strata (dip range from 12° to 25°), (10) main landslide scarp, (11) Güevejar landslide mass, (12) trace of geological cross section, (13) seismometric station, (14) seismic array, (15) ReMi and (16) borehole.

Diezma landslide

The Diezma landslide is located 25 km NE of the city of Granada; although the slope had repeatedly suffered small-scale stability problems since the construction of the A-92 highway, a larger failure occurred on 2001 March 18, causing damage in several locations (Azañón *et al.* 2010; Rodríguez-Peces *et al.* 2011; Delgado *et al.* 2015). The landslide had a main translational mechanism and involved an estimated volume of 1.2 Mm^3, composed of a chaotic deposit of silt and clay with heterometric blocks of limestone ascribable to the Numidoide Formation (Aquitanian-Burdigalian). Despite the 18 million Euros spent since 1999 on geotechnical investigations and stabilization solutions (Delgado *et al.* 2015), the numerous reactivations that occurred through 2013 demonstrate the persistency of the landslide activity.

Delgado *et al.* (2015) proposed an engineering-geological model for this landslide (Figs 4b and 6). For their study, they employed stratigraphic logs of 34 boreholes drilled in several campaigns from 1999 to 2012 and correlated them. These data were also correlated with ground surface observations. As can be observed from a geological cross-section reconstructed along the slope, the landslide involves the Numidoide Formation only, and the sliding surface has a maximum depth of 25 m. Based on specifically performed downhole tests (Fig. 5) as well as *f–k* array and MASW data, available from technical reports owned by the Junta de Andalusia administration, an average *Vs* of 300 m s^{-1} can be attributed to the landslide mass, while the seismic bedrock corresponds to the Numidoide Formation, as it is characterized by *Vs* higher than 750 m s^{-1} (Table 1).

SEISMIC MEASUREMENTS FOR LOCAL SEISMIC RESPONSE

Güevejar

Several geophysical campaigns of seismic noise were performed in the Güevejar landslide site over three years starting in September 2011 to investigate the main resonance frequency (f_{res}) of the landslide debris overlaying the stiff bedrock. If a theoretical 1-D resonance model is assumed, the expected f_{res} value corresponds to the ratio *Vs*/4H, that is related to the thickness (*H*) as well as to the seismic wave velocity (*Vs*) of the landslide mass; nevertheless, if 2-D local amplification conditions exist, they can significantly modify the theoretical f_{res} value (Semblat *et al.* 2002a,b). The 45 noise stations were equipped with a Guralp CMG-6TD three-component broadband seismometer, and the records were processed by GEOPSY software (release 2.7.4; Whatelet *et al.* 2011) according to the SESAME Working Group (2004) standards. The horizontal over vertical spectral ratios (HVSR) were derived according to the approach of Nakamura (1989), as well as the HVSR azimuthal distribution. The noise measurements have an average duration of 30 min and were repeated at different hours and days; moreover, for a part of the stations, the measurements were also repeated by recording continuously for 5 hr. The stations were distributed within and outside the landslide mass; nevertheless, as seen from the data processing, no HVSR peaks can be observed, neither in the landslide area nor outside. Based on these results, no stratigraphic resonance can be associated with the landslide mass.

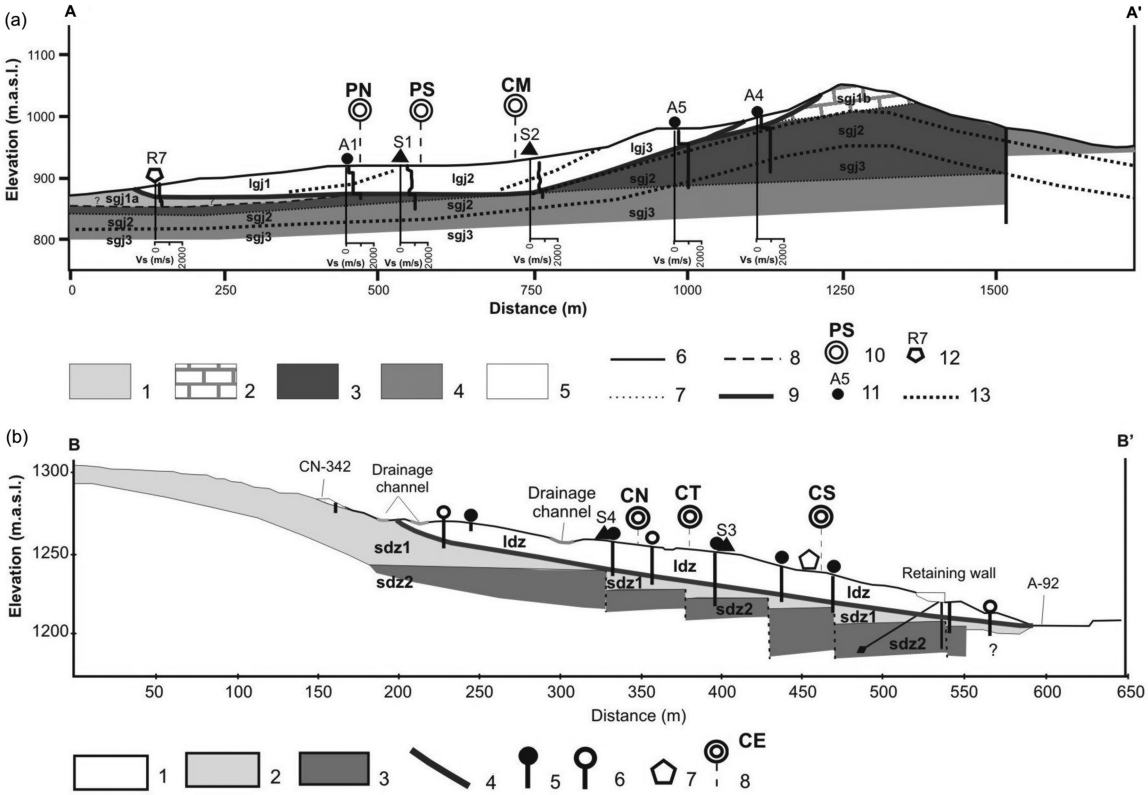

Figure 4. (a) Geological cross-section of the Güevejar landslide. Labels of the lithotechnical units of Table 1 are also reported: (1) red silts, sandstones and conglomerates (Plio-Pleistocene), (2) Lacustrine limestone and marls (upper Miocene), (3) red silts with cemented conglomerates (upper Miocene), (4) grey clays with gypsum, silts and marls with lignite (upper Miocene), (5) Güevejar landslide mass, (6) fault, (7) conformity, (8) unconformity, (9) sliding surface of the landslide, (10) seismometric station of the temporary array, (11) seismic array, (12) ReMi, (13) seismo-strata limits. *Vs* (m s^{-1}) profiles from ReMi are also projected along the section. (b) Geological-cross section of the Diezma landslide. Labels of the lithotechnical units of Table 1 are also reported: (1) Diezma landslide mass, (2) *Numidoide* Formation (Aquitanian-Burdigalian), (3) Formations of the *Maláguide* domain (Devonian – Triassic), (4) sliding surface of the landslide, (5) borehole, (6) inclinometer, (7) seismic array and (8) seismometric station of the temporary array.

Table 1. Dynamic properties of the lithotechnical units distinguished in the Güevejar and Diezma landslide areas (see Fig. 4) and derived from *in situ* geophysical investigations.

Landslide	Model unit	*Vs* (m s^{-1})	den (kg m^{-3})	*G* (Pa)	*v*	*E* (Pa)	*K* (Pa)
Guevejar	lgj1	370	1900	2.60E+08	0.36	7.07E+08	8.42E+08
Guevejar	lgj2	700	1900	9.31E+08	0.36	2.53E+09	3.01E+09
Guevejar	lgj3	335	1900	2.13E+08	0.36	5.80E+08	6.90E+08
Guevejar	sgj1a	450	2000	4.05E+08	0.40	1.13E+09	1.89E+09
Guevejar	sgj1b	900	2000	1.62E+09	0.40	4.54E+09	7.56E+09
Guevejar	sgj2	950	2000	1.81E+09	0.40	5.05E+09	8.42E+09
Guevejar	sgj3	1000	2100	2.10E+09	0.25	5.25E+09	3.50E+09
Diezma	ldz	300	1890	1.70E+08	0.25	4.25E+08	2.84E+08
Diezma	sdz1	800	2044	1.31E+09	0.25	3.27E+09	2.18E+09
Diezma	sdz2	1000	2331	2.33E+09	0.25	5.83E+09	3.89E+09

A temporary seismometric array was also installed in the landslide area (Fig. 3), composed of four stations within the landslide mass (CM, PN, PS and GR), a station very close to the eastern flank of the landslide (MN) and one reference station (*sensu* Borcherdt 1994) located outside the landslide mass on outcropping bedrock (CG). The array operated from May 2012 until February 2013, recording 40 earthquakes (Table 2), with M_w ranging from 1.1 to 8.0 and epicentral distances varying from 12 up to thousands of km, and 24 earthquakes were recorded at the reference station (CG). The recorded earthquakes were processed to obtain receiver functions, HVSR (Field & Jacob 1995), and standard spectral ratios, SSR (Borcherdt 1994), to the reference station. The receiver functions (Fig. 7) are in very good agreement with the HVSRs from the 5-hr noise records and confirm that no significant seismic peaks due to stratigraphic resonance exist in the landslide area. The SSRs (Fig. 8) indicate that significant amplification exists between 3 and 5 Hz, which becomes more intense upon moving from the upper to the lower portion of the landslide mass (i.e. from CM to PS and PN) and from the internal portion to the flanks (i.e. from CM to GR and from PS to MN).

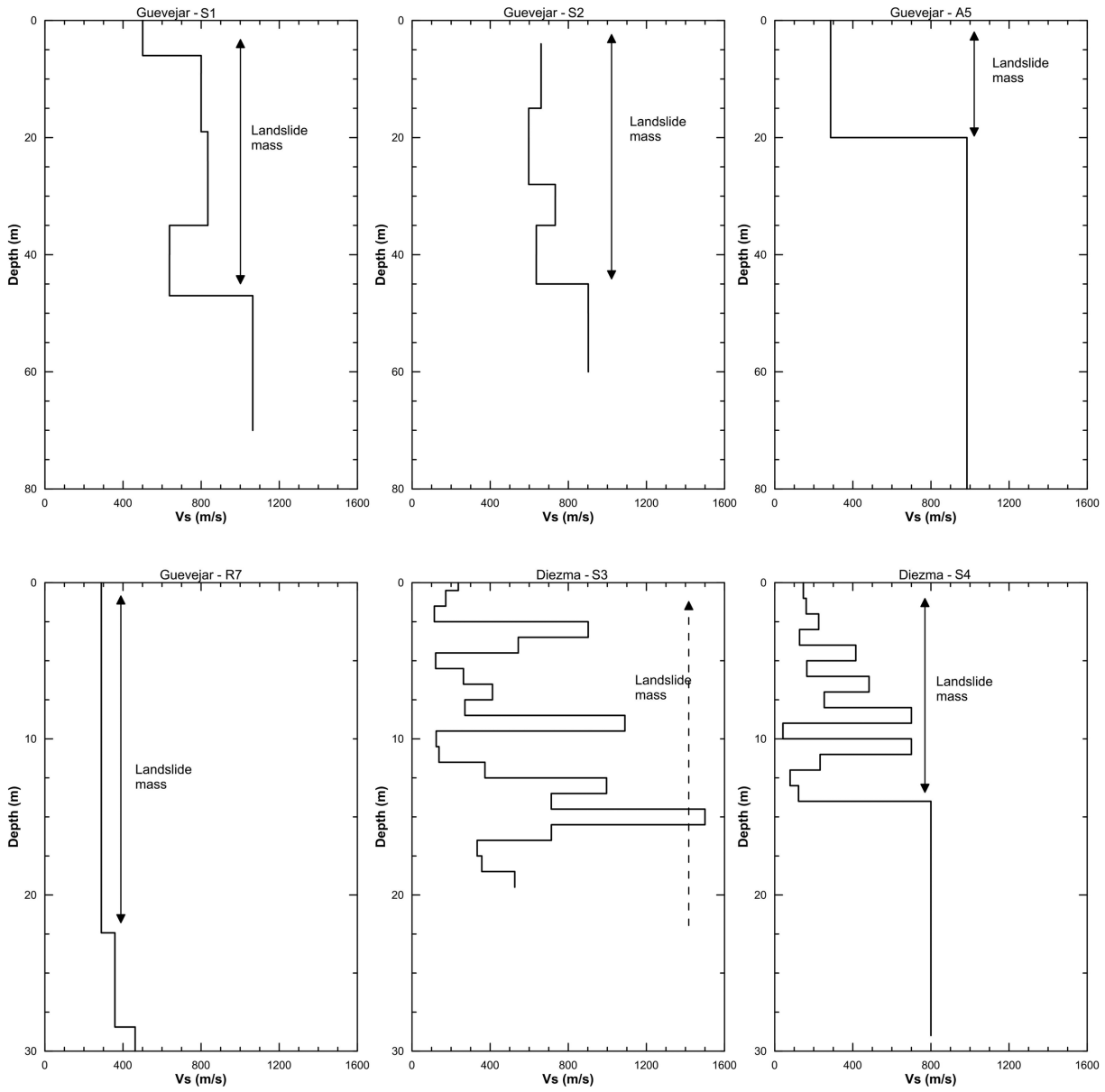

Figure 5. *Vs*-logs derived from borehole tests specifically performed at Güevejar (S1, S2) and Diezma (S3, S4) landslides. The results of ReMi R7 and *f–k* array A5 performed at Güevejar are also reported. See Figs 3, 4 and 6 for data locations.

Diezma

Three geophysical campaigns of seismic noise measurements were performed in the Diezma landslide slope since November 2012. The 28 measurement stations (Fig. 9) were equipped with a Guralp CMG-6TD three-component broadband seismometer. The noise records have an average duration of 45 min and were collected during night hours to avoid disturbances due to highway traffic (Delgado *et al.* 2015). The seismic noise records were processed by GEOPSY software (release 2.7.4; Whatelet *et al.* 2011) according to the SESAME Working Group (2004) standards. The HVSRs were derived according to the approach of Nakamura (1989), as well as the HVSR azimuthal distribution.

The analysis of the noise records (Fig. 9) demonstrates that the landslide mass is characterized by a clear resonance frequency in the range of 4–5 Hz that is not present outside the landslide mass. Moreover, the HVSR amplitudes generally decrease from the middle portion of the landslide mass towards the boundaries and are significantly reduced at the bottom of the slope, where a lower impedance contrast can be related to the rock fill behind the concrete wall that was constructed in 2001 to stabilize the roadway trench. Based on the azimuthal HVSR graphs of Fig. 9, no significant anisotropy of ambient noise field can be observed in the landslide mass.

Moreover, considering the mid-slope position of the landslide mass and the slope inclination angle lower than 15°, topographic amplification/de-amplification effects can be neglected with respect to the resonance of the landslide mass itself (Lenti & Martino 2012, 2013). Based on the peak frequencies retrieved from the noise and the landslide thickness from the engineering-geology model, the landslide mass should be characterized by a *Vs* value of approximately 300 m s^{-1}. This value is confirmed by downhole measurements performed specifically for this study in the landslide area, compared to the available MASW (Fig. 5). Similarly to the Güevejar test site, a temporary seismometric array was installed on

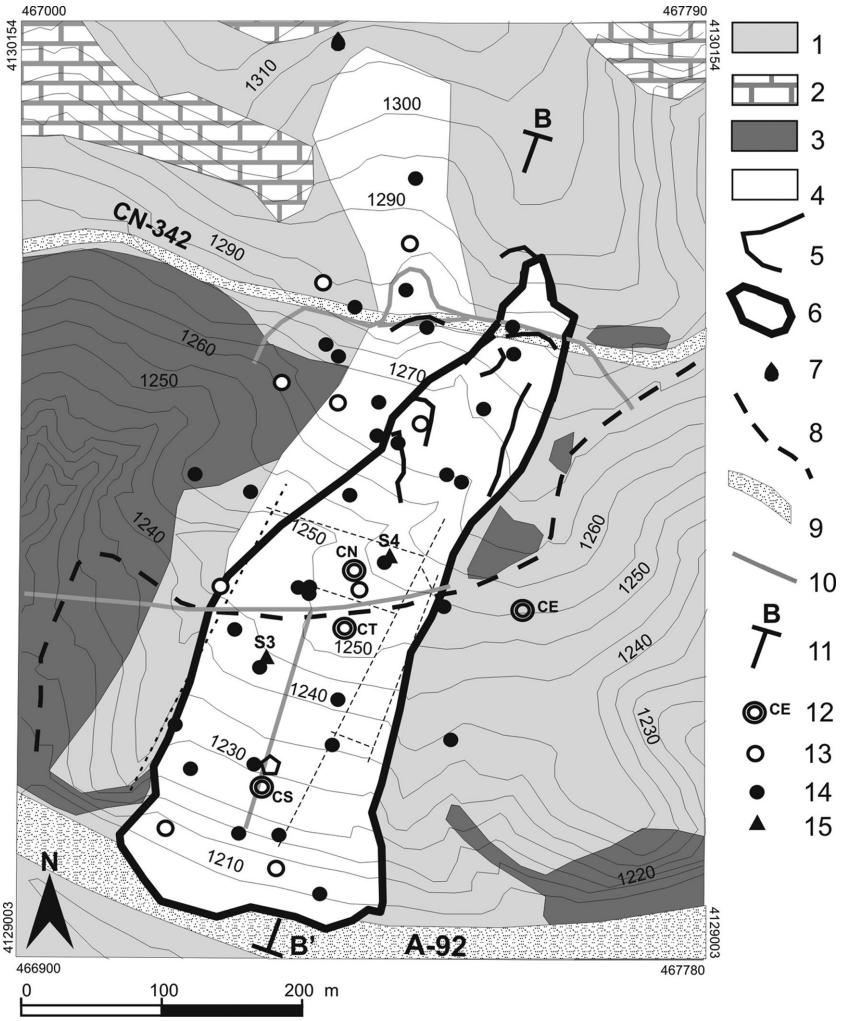

Figure 6. Geological map of the Diezma landslide area (the geographic coordinates are provided in UTM-ETRS89 reference system): (1) *Numidoide* Formation (Aquitanian-Burdigalian), (2) Limestones of the *Dorsal* domain (Eocene), (3) Formations of the *Maláguide* domain (Devonian – Triassic), (4) slope and landslide debris, (5) ground cracks observed since 1998, (6) Diezma landslide mass, (7) spring, (8) track, (9) main roads, (10) drainage line, (11) trace of geological cross section, (12) seismometric station, (13) inclinometer, (14) borehole (1999–2009), (15) new boreholes (2012).

the landslide slope to evaluate the local seismic response by using the receiver functions, HVSR (Field & Jacob 1995), and the standard spectral ratios, SSR (Borcherdt 1994), from weak motions (Fig. 6).

In addition, four seismometric stations were equipped with Guralp CMG-6TD three-component broadband seismometers connected to GPS for absolute timing. These stations were active for almost 7 months (from June 2013 to December 2013); three stations (CN, CT and CS) were located within the landslide mass, and the last one was outside in a reference site (CE), that is characterized by outcropping bedrock and without seismic amplification as occurred in the noise measurements. This temporary array recorded 17 earthquakes in total (Table 3), with M_w ranging from 2.1 to 7.3 and epicentral distances varying from 13 to thousands of km. Both the HVSRs and the SSRs (Fig. 10) confirm the evidence resulting from the noise HVSRs: (i) a significant seismic amplification exists within the landslide mass at 3–5 Hz, (ii) lower amplification levels correspond to the southern portion of the mass, which is located at the bottom of the slope and (iii) no amplification exists outside the landslide mass.

NUMERICAL MODELS

2-D numerical modelling was performed by the finite difference code FLAC 7.0 (Itasca 2011), that is adopting an explicit time-marching solution in double precision. The FLAC formulation is conceptually similar to that of dynamic relaxation proposed by Otter *et al*. 1966, with adaptations for arbitrary grid shapes, large strains and different damping. The finite difference scheme follows the approach of Wilkins (1964). Modelling was performed to simulate the local seismic response (LSR) of the two landslide slopes as a preliminary stage before evaluating the expected landslide mass mobility (LMM) under dynamic conditions. The collected geophysical data were taken into account to validate the numerical outputs; the engineering-geological models, reconstructed along the landslide masses, were transposed into numerical domains. More in particular, a square grid (800 × 180) with a resolution of 2.5 m and a square grid (573 × 210) with a resolution of 1.5 m were used for the Güevejar and Diezma landslides, respectively. The adopted resolutions are suitable to obtain a corresponding maximum admissible frequency for the model $f = V_S/(n\Delta l)$ (Kuhlemeyer & Lysmer 1973), where V_S is the minimum shear wave velocity, Δl is the

Table 2. Earthquake recorded by the temporary seismometric array at Güevejar. The recording stations are also reported. The data sources are IGN (Instituto Geográfico Nacional, Spain); INGV (Istituto Nazionale di Geofisica e Vulcanologia, Italy); USGS (United States Geological Survey, US); and NEIC (National Earthquake Information Center, US).

No.	Source area	Date (dd/mm/yyyy)	Time (GMT)	Magnitude	Epicentral distance (km)	Data source	CG	MN	CM	GR	PN	PS
1	Mirandola (Italy)	20/05/2012	02:03:00	5.9	>1000	INGV	x	x	x			x
2	Norway Sea	24/05/2012	22:54:00	6.1	>1000	USGS	x	x	x	x		x
3	Mirandola (Italy)	29/05/2012	07:03:00	5.8	>1000	INGV	x	x	x	x	x	x
4	Mirandola (Italy)	29/05/2012	10:59:00	5.3	>1000	INGV	x	x	x	x		x
5	W Padul (Spain)	07/06/2012	05:50:00	2.3	30	IGN	x	x	x	x	x	x
6	NW Arboleas (Spain)	07/06/2012	10:27:00	3.5	130	IGN	x	x	x	x	x	x
7	SW Agrón (Spain)	19/06/2012	01:28:00	3.2	40	IGN	x	x	x	x	x	x
8	Dushanzi (China)	29/06/2012	21:07:00	6.3	>1000	USGS	x	x	x			x
9	El Salvador, offshore	27/08/2012	04:37:00	7.3	>1000	USGS	x		x			
10	Jan Mayen (Norway)	30/08/2012	13:43:00	6.8	>1000	USGS	x		x			
11	Phillipines	31/08/2012	12:47:00	7.6	>1000	USGS	x		x			
12	Costa Rica	05/09/2012	10:04:48	7.6	>1000	USGS	x		x			
13	N Alborán Sea	06/09/2012	04:24:00	3.4	70–100	IGN	x		x			
14	SE Jayena (Spain)	07/09/2012	18:10:00	3.0	40–55	IGN	x		x			
15	E Jódar (Spain)	20/09/2012	19:05:00	2.9	58–67	IGN	x		x			
16	Charlotte Island (Canada)	28/10/2012	03:04:00	7.7	>1000	USGS	x	x	x			x
17	NE Purchil (Spain)	04/11/2012	02:43:00	1.1	12	IGN		x	x			x
18	Guatemala offshore	07/11/2012	16:35:00	7.4	>1000	USGS		x	x			x
19	N Alborán Sea	11/11/2012	00:19:00	3.3	110	IGN		x	x			x
20	Honshu E coast (Japan)	07/12/2012	08:18:00	7.3	>1000	NEIC		x	x	x		x
21	W Torreperogil (Spain)	15/12/2012	18:59:00	3.7	88	IGN	x	x	x	x		x
22	NW Torreperogil (Spain)	16/12/2012	04:09:00	3.6	89	IGN	x	x	x	x		x
23	NW Torreperogil (Spain)	17/12/2012	05:34:00	3.6	89	IGN	x		x	x		x
24	NE Sabiote (Spain)	17/12/2012	23:33:00	2.8	93	IGN			x	x		x
25	SE Sabiote (Spain)	17/12/2012	23:36:00	2.9	90	IGN			x	x		x
26	NE Torreperogil (Spain)	17/12/2012	23:47:00	2.9	90	IGN			x	x		x
27	SE Sabiote (Spain)	17/12/2012	23:49:00	2.7	90	IGN			x	x		x
28	E Sabiote (Spain)	18/12/2012	03:20:00	2.7	92	IGN			x	x		x
29	E Sabiote (Spain)	18/12/2012	03:32:00	2.9	91	IGN			x	x		x
30	W Torreperogil (Spain)	18/12/2012	03:36:00	2.7	87	IGN			x	x		x
31	NE Alcaucín (Spain)	21/12/2012	00:23:00	3.8	61	IGN	x		x	x		x
32	NW La Malahá (Spain)	30/12/2012	00:08:00	1.8	21	IGN			x	x		x
33	SE Alaska (USA)	05/01/2013	08:58:00	7.5	>1000	USGS			x	x		x
34	E Gergal (Spain)	09/01/2013	07:27:00	3.4	99	IGN	x		x	x		x
35	SW Montillana (Spain)	09/01/2013	23:27:00	3.9	27	IGN	x		x	x		x
36	NW Torreperogil (Spain)	05/02/2013	15:18:00	3.2	88	IGN		x	x	x		x
37	NE Torreperogil (Spain)	05/02/2013	21:24:00	3.7	89	IGN	x	x	x	x		x
38	SE Sabiote (Spain)	06/02/2013	00:06:00	3.0	89	IGN		x	x	x		x
39	New Hebrides Islands	06/02/2013	01:12:00	8.0	>1000	NEIC	x	x	x	x		x
40	E Siberia	14/02/2013	13:13:00	6.9	>1000	NEIC		x	x	x		x

maximum nodal distance within the model, which is consistent with the frequency range of interest, and n is the number of nodes per wavelength, varying from 6 up to 10. The total width and height of the mesh are greater than twice the dimension of the slope to minimize the effects of artificial wave reflections from the boundaries. Quiet boundary conditions were applied at the base of the mesh (Kuhlemeyer & Lysmer 1973), and free-field conditions were applied at the lateral boundaries (Cundall *et al*. 1980).

For each model, an initial geostatic stress field was computed with the assumption of strain-plane conditions; in the dynamic configuration, the seismic inputs were applied in the form of vertical upward-propagating SV stress waves.

With respect to the rheology used, non-linear unstable dynamic behaviour was modelled considering more conservative perfectly plastic conditions controlled by a Mohr–Coulomb yield criterion, that is by assuming that the limit state conditions were related to the strength properties of the soil. According to the literature (Cetin *et al*. 2004; Zhai *et al*. 2004; Lenti & Martino 2013), this solution is reliable because a generalized rheological model for simulating non-linear unstable conditions under dynamic conditions (i.e. out of the non-linear stable strain range) is not yet available for finite difference numerical solutions, so the generation of pore water pressures and the consequent dependence of the damping on the number of dynamic cycles were not considered here.

Moreover, if the local stress results are lower than the volumetric threshold, a viscous rheology was implemented by two different stress strain behaviours: (1) a linear behaviour (VL), assuming constant values for both stiffness (G) and damping (D) and (2) a non-linear behaviour (VNL), solved by taking into account the decay of the G value and the increase of the D value corresponding to the strain level.

Towards this aim, specific laboratory tests were performed at the IFSTTAR laboratory (Paris, Marne la Vallé - France) and at the Engineering Geology laboratory of the Department of Earth Sciences of the University of Rome "Sapienza" (Rome, Italy) on samples from the Upper Miocene red silts of the Güevejar landslide site

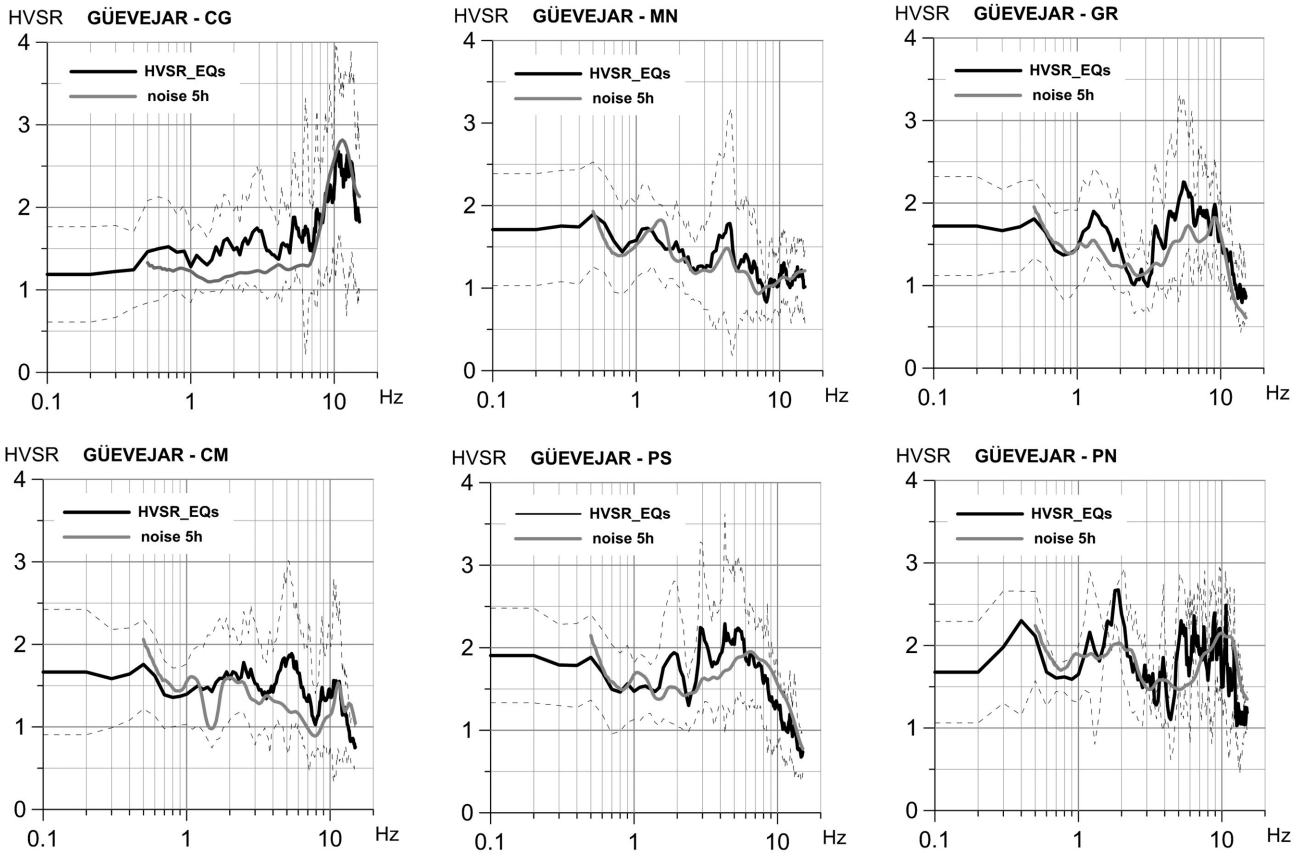

Figure 7. Average HVSRs +/– standard deviations obtained from earthquakes recorded by the Güevejar temporary seismometric array. The HVSRs from 5-hr noise measurements are also reported.

and from the *Numidoide* Formation of the Diezma landslide site. As a result of these tests, the sample from the Upper Miocene red silts of Güevejar site are classified as low-compressibility clay (CL) according to the Unified Soil Classification System (USCS), with a liquid limit of 30.3 per cent and a plasticity index of 15.1 per cent, while the sample from the *Numidoide* Formation of Diezma is classified as high-compressibility clay (CH) following the USCS classification, with a liquid limit of 52.5 per cent and a plastic index of 26.7 per cent. Shear strength parameters were derived for isotropically confined drained triaxial tests (CDI-TX) and isotropically confined drained triaxial tests (CUI-TX) following the standard ASTM D4767-04 (2000). For the red silts of Güevejar, the friction angle and cohesion from CDI-TX are 20° and 0 kPa, while those from CUI-TX are 9° and 50 kPa. For the *Numidoide* Formation of Diezma, strength parameters are already available from literature data (Delgado *et al*. 2015). Dynamic tests were performed at the resonant column (RC) following the standard ASTM D4015-92 (2000); the samples were isotropically confined in the pressure range 50–200 kPa, representing the *in situ* lithostatic conditions, and the decay curves obtained for the normalized shear modulus (G/G_0) and percentage damping (D per cent) are reported in Fig. 11. According to these tests, the initial dynamic shear moduli (G_0) at 200 kPa are 91 MPa ($Vs_0 = 232$ m s^{-1}) and 63 MPa ($Vs_0 = 177$ m s^{-1}) for the red silts of Güevejar and the Numidoide Formation of Diezma, respectively.

Energy dissipation was computed using a Rayleigh damping function (Zienkiewicz 2005; Semblat & Pecker 2009) and defining a viscosity matrix (C) as a linear combination of a mass-dependent term and a stiffness-dependent term in the form

$$C = \alpha M + \beta K, \tag{1}$$

where α is the constant for the mass matrix (M), and β is the constant for the stiffness matrix (K). This dissipation function implies a minimum damping at the circular frequency

$$\omega_{\min} = (\alpha/\beta)^{1/2}, \tag{2}$$

for which the subsequent damping is

$$\xi_{\min} = (\alpha\beta)^{1/2}.$$

The minimum circular frequency, $\omega_{\min}$, corresponds to the minimum of the Rayleigh damping function, while the value of the minimum damping, $\xi_{\min}$ (equal to $(2Q_{\max})^{-1}$, where Q is the quality factor of the material), varies as a function of the shear strain according to the adopted dynamic behaviour of the soil. According to laboratory tests, in the case of Güevejar, the assumed $\xi_{\min}$ for the VL rheology is 0.008 and 0.05 for the bedrock and soft soils, respectively, and in the case of Diezma, the assumed $\xi_{\min}$ for the VL rheology is 0.005 and 0.02 for the bedrock and soft soils, respectively. For the VNL rheology, the ξ for the soft soil varies up to 0.2, depending on the strain level. For both the VL and VLN rheologies, the $\omega_{\min}$ was fixed at 3 to guarantee an almost flat Rayleigh damping function in the frequency range of interest (1–10 Hz).

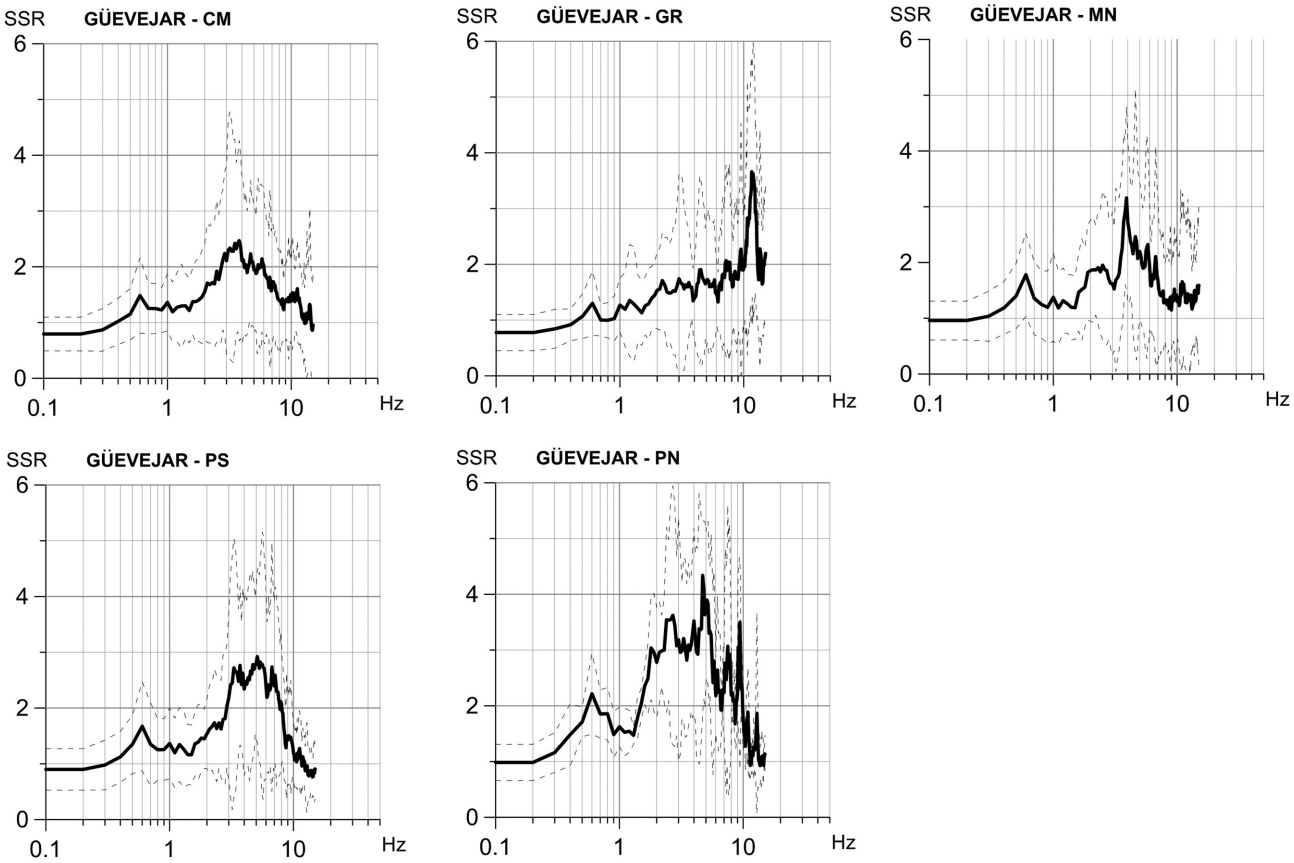

Figure 8. Average SSRs +/– standard deviations obtained from the earthquakes recorded by the Güevejar temporary seismometric array.

LSR modelling

In the case of the Güevejar landslide the LSR 2-D numerical modelling was carried out under two conditions: (i) considering a homogeneous bedrock only and (ii) considering the presence of the landslide mass and the local geological setting. The first condition was assumed to investigate only the effects due to the hill slope topography. The numerical amplification function $A(f)$ was computed at each grid node of the numerical domain surface by the spectral ratio between the local numerical accelerometric output and that considered on the outcropping bedrock (i.e. selected close to the latter boundary of the model). The $A(f)$ values were contoured all along the surface of the numerical domain to obtain an $A(f)_x$ distribution (Fig. 12). If the geological setting is considered, seismic amplification results in correspondence to the landslide mass in the wide 1.5–4 Hz frequency range (Fig. 12a). Fig. 13 shows the normalized SSRs obtained from recorded earthquakes and from numerical modelling to better compare the shape of the amplification functions. As it results, the SSRs from numerical modelling are in very good agreement with the SSRs from earthquakes at stations PN and PS, representative of the internal portion of the landslide mass (Fig. 13). On the other hand, the numerical results at the same stations show significant differences from those derived by the SSRs at frequencies lower than 1.5 Hz; this output can be justified by considering the $A(f)_x$ function and the particular location of the considered stations, which is between the lower and middle portions of the landslide mass. Based on the 2-D modelling, a relevant decrease in $A(f)$ can be observed moving upslope from PN to PS at lower frequencies (<2 Hz); nevertheless, a best fit could be probably reached by introducing a further lower-impedance contrast zone below the secondary sliding surface located between PN and PS. Because such a solution could not be supported by the geological evidence as well as by the available geophysical data, it was preferred not to force the model towards an only numerical convergence solution. In the case of the homogeneous domain, a low-amplification effect is visible in a 2–4 Hz frequency range at the hill top and in correspondence to the flat counterslope due to the main terrace of the landslide (Fig. 12b). Several deamplification bands are also visible in the $A(f)_x$ function, where the hill slope inclination increases to approximately 25°.

In the case of the Diezma landslide, the 2-D LSR numerical modelling was performed only by considering the complex geological setting of the slope, as no significant amplification can be expected for the gently dipping topography. The resulting $A(f)_x$ (Fig. 14) reveals high amplification in correspondence to frequency ranges that significantly vary upon moving from the top (4–8 Hz) to the middle (3–5 Hz) to the base (4–10 Hz) of the slope. In this case, also, the numerical amplification functions are in good agreement with the SSRs from the earthquake, in particular for stations CN, CT and CS, located at the top, middle and base zones of the slope, respectively (Fig. 13).

LMM numerical analysis

The LMM analysis under dynamic conditions was performed by applying several inputs to the numerical models of both the Güevejar and Diezma landslides and computing the displacement fields induced within the landslide mass. Towards this aim, a customized script written for managing the numerical results distinguished

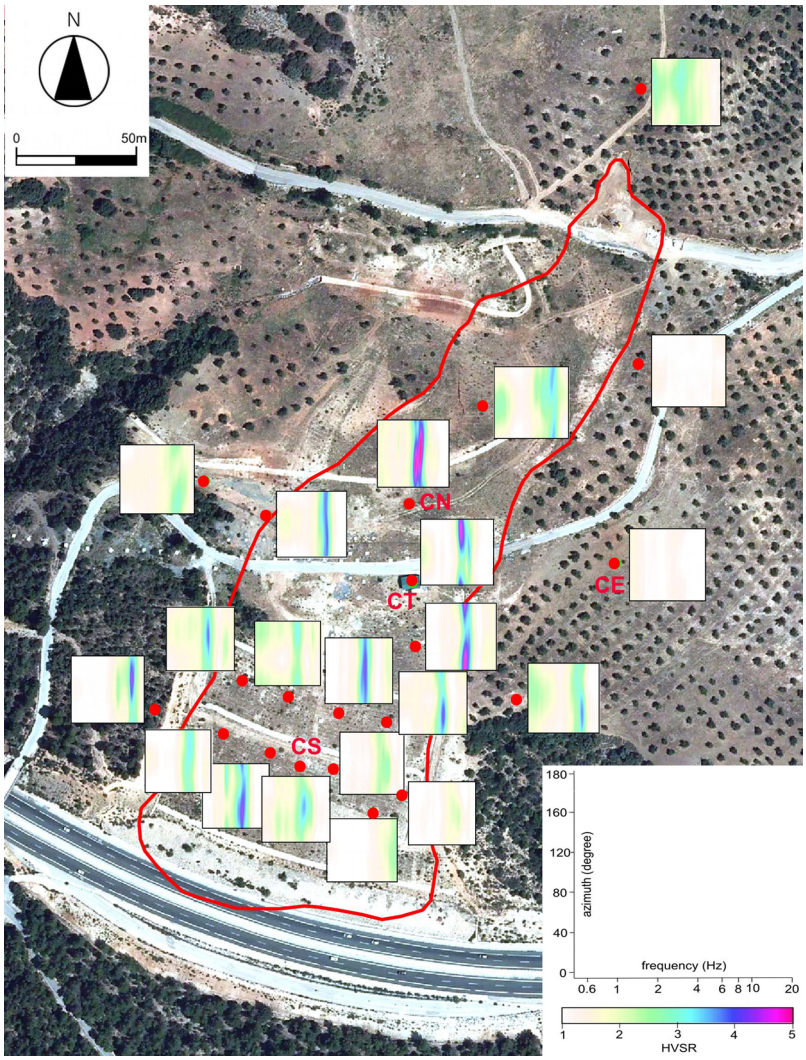

Figure 9. Location of the noise measurements performed in the Diezma landslide area on a Google Earth satellite view (modified from Delgado *et al*. 2015). The HVSR-rotate plots and standard outputs (SESAME 2004) from GEOPSY software are also reported.

Table 3 Earthquake recorded by the temporary seismometric array at Diezma. The recording stations are also reported. The data sources are IGN (Instituto Geográfico Nacional, Spain); ISC (International Seismological Center); an CSEM (European-Mediterranean Seismological Centre).

n°	Souce area	Date (dd/mm/yyyy)	Time (GMT)	Magnitude	Epicentral distance (km)	Data source	CE	CT	CN	CS
1	N Alborán Sea	23/06/2013	02:04:38	2.9	118	IGN	x	x	x	x
2	NW Benalúa de las Villas	28/07/2013	23:57:42	3.0	36	IGN	x	x	x	
3	NE Torres de Alcala	08/08/2013	07:05:25	3.7	237	IGN	x	x	x	x
4	W Santa Cruz del Comercio	08/08/2013	07:25:38	2.4	64	IGN	x	x	x	x
5	N Fines (Spain)	10/08/2013	13:07:30	3.1	98	IGN	x	x	x	x
6	SE La Mamola (Spain)	11/08/2013	12:33:42	3.3	59	IGN	x	x	x	x
7	N Alborán Sea	14/08/2013	19:24:13	3.4	116	IGN	x	x	x	x
8	NE Jayena (Spain)	19/08/2013	18:46:14	2.4	50	IGN	x	x	x	x
9	E Iznalloz (Spain)	22/08/2013	00:28:04	1.7	13	IGN	x	x	x	x
10	Crete (Greece)	12/10/2013	13:11:56	6.5	>1000	ISC	x	x	x	
11	SE Torreperogil (Spain)	19/10/2013	15:54:21	3.6	80	IGN	x	x	x	x
12	SE Torreperogil (Spain)	19/10/2012	17:31:54	3.1	79	IGN	x	x	x	x
13	W Jerez del Marquesado (Spain)	23/10/2013	05:22:14	2.1	20	IGN	x	x	x	x
14	SW Cabo de San Vicente (Spain)	23/10/2013	13:57:27	4.5	600	IGN	x	x	x	x
15	Honshu E coast (Japan)	25/10/2013	17:10:16	7.4	>1000	ISC	x	x	x	x
16	SE Atarfe (Spain)	16/11/2013	06:15:33	2.4	30	IGN	x	x	x	x
17	Scotland Sea	17/11/2013	09:04:55	7.3	>1000	CSEM	x	x	x	x
18	W Alboran Sea	05/12/2013	15:47:08	3.5	131	IGN	x	x	x	x
19	Cadiz Gulf	16/12/2013	07:06:23	4.9	375	IGN	x	x	x	

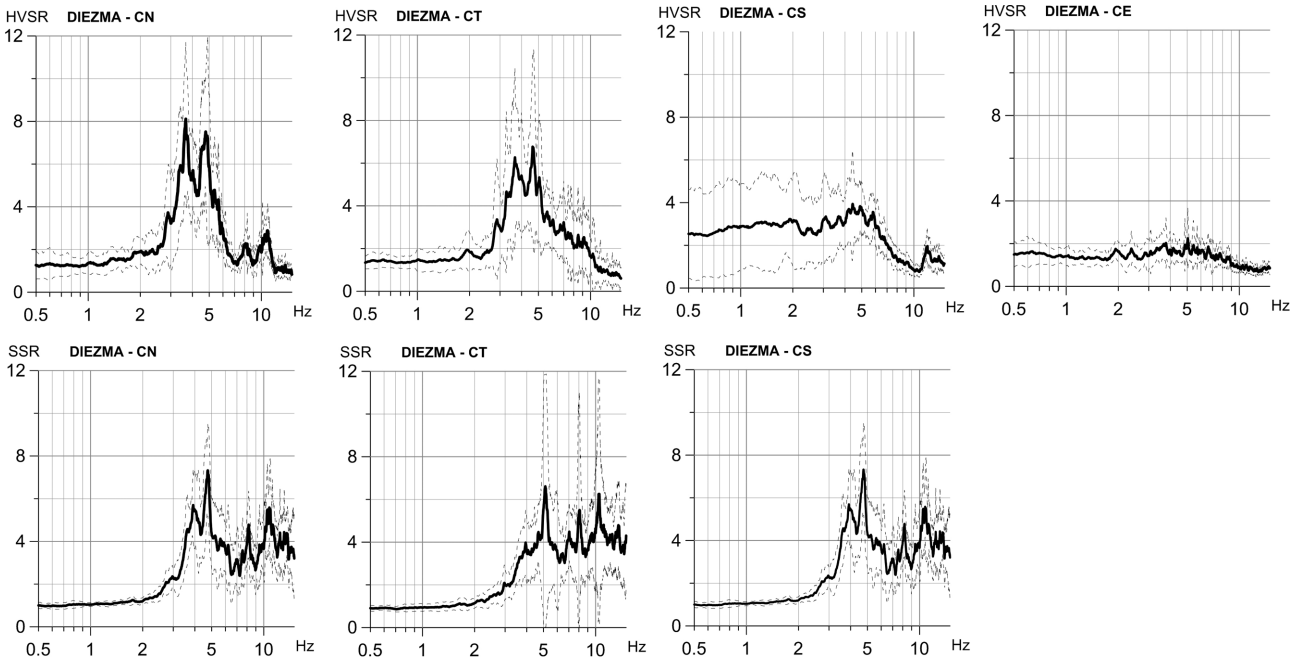

Figure 10. Average HVSRs +/– standard deviations obtained from the earthquakes recorded by the Diezma temporary seismometric array (upper row). Average SSRs +/– standard deviations obtained from the earthquakes recorded by the Diezma temporary seismometric array (lower row).

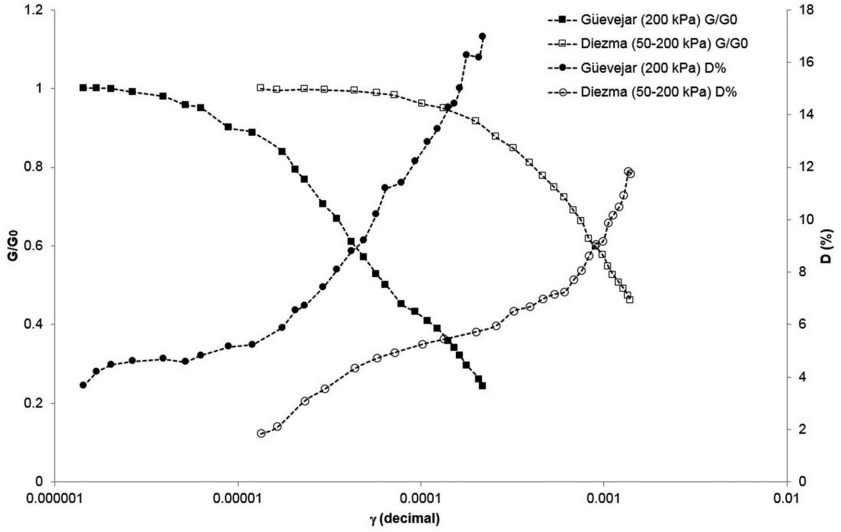

Figure 11. Normalized decay curves, G/G_0 and D/D_0, obtained from resonant column tests performed at the IFSTTAR laboratory on the red silts (black symbols) and on the *Numidoide Formation* (white symbols) sampled from the Güevejar and Diezma landslide areas, respectively.

between the displacements inside and outside the landslide mass and computed the movement to quantify the effective horizontal displacement (*x*-disp) with respect to the substratum. Moreover, according to Lenti & Martino (2013), the *x*-disp values were defined considering different percentages of the landslide mass with the largest displacements (i.e. 5, 15, 30, 50 and 100 per cent).

The seismic inputs for the numerical models were derived by selecting 15 accelerometric records of the European database integrated with records from the K-NET and COSMOS databases (Table 4). These inputs are characterized by the Arias intensity (AI) on the order of 0.01 m s^{-1} and different values of the characteristic period, T_m, ranging from 0.3 to 16.5 s. Depending on the proper landslide dimensions, the computed T_s is equal to 0.5 and 0.2 s for the Güevejar and Diezma landslides, respectively, while T_l is equal to 2.6 and 1.3 s. As a consequence, the values of the T_s/T_m ratio are in the range of 0.03–2.63 for the Güevejar landslide and 0.05–2.5 for the Diezma landslide, while the values of the T_l/T_m ratio are in the ranges of 0.16–13.68 and 0.33–16.63, respectively.

To perform the LMM analysis, the time histories of the selected inputs were scaled to have AI values of 0.001 and 1 m s^{-1} without modifying the T_m; in this way, 36 inputs where available for each landslide, representative of three energy levels in a wide range of T_m values. Moreover, to perform the dynamic modelling, an equivalent signal was associated with each selected input according to the LEMA_DES (Levelled-Energy Multifrequential Analysis

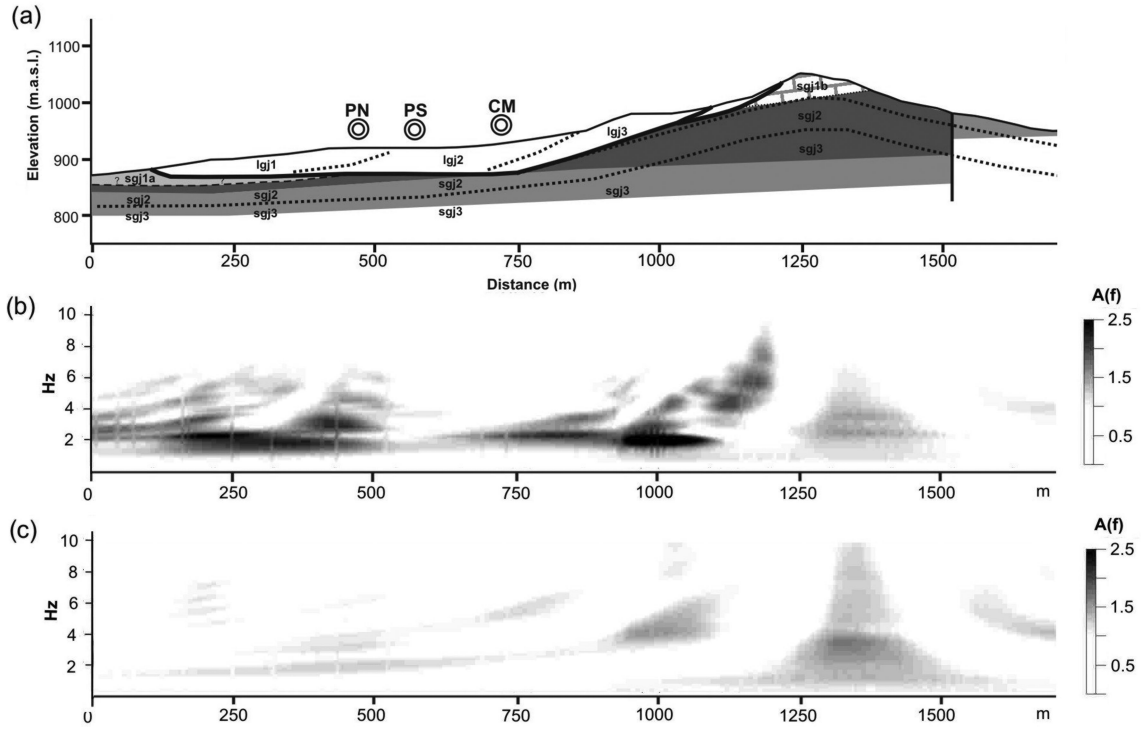

Figure 12. (a) Engineering-geological cross-section of the Güevejar landslide (see Fig. 4a for the legend); $A(f)_x$ functions obtained by LSR 2-D numerical modelling of the Güevejar landslide slope by considering the local geological setting (b) and the homogeneous slope (c). Location of receivers are mapped in Fig. 3.

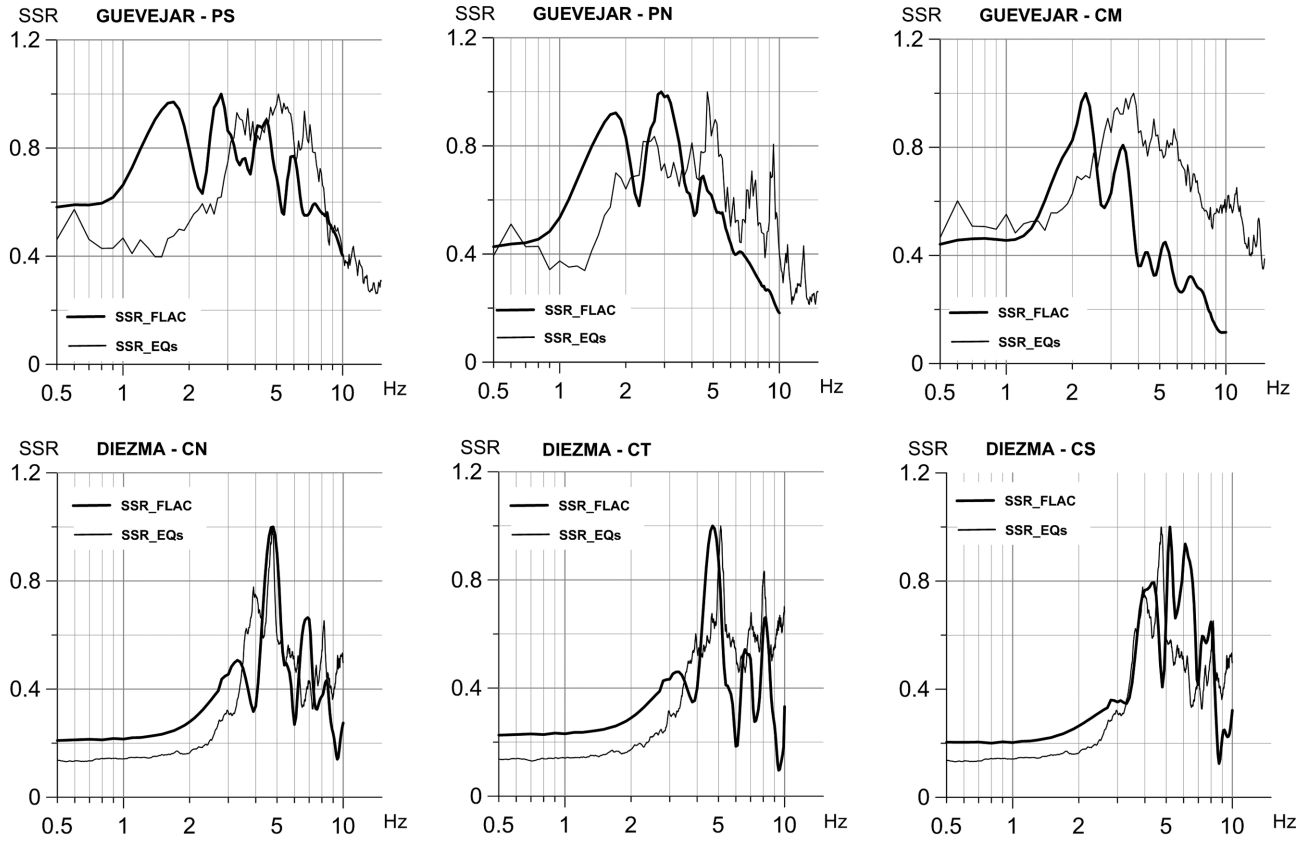

Figure 13. Numerical $A(f)$ by FLAC compared with the SSRs from earthquake records at Güevejar (upper row) and Diezma (lower row) landslides. Locations of receivers are reported in Figs 3 and 6 for Güevejar and Diezma, respectively.

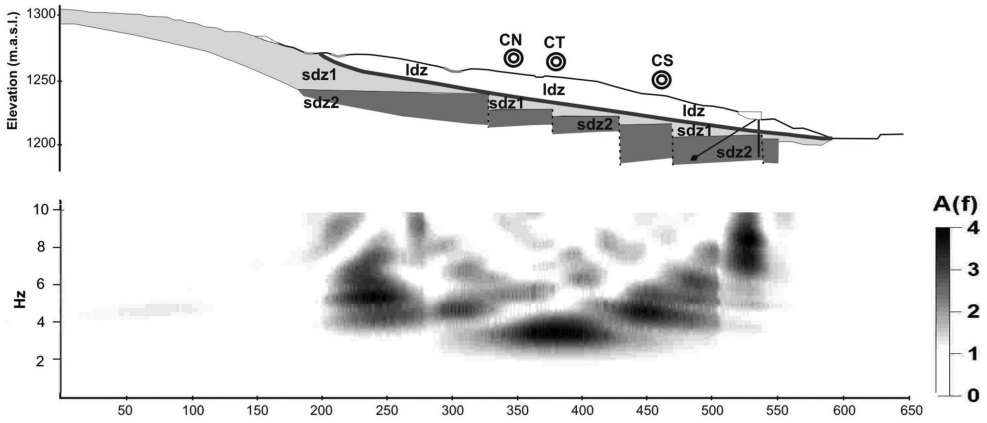

Figure 14. (a) Engineering-geological cross-section of the Diezma landslide (see Fig. 4b for the legend); $A(f)_x$ function obtained by LSR 2-D numerical modelling of the Diezma landslide slope by considering the local geological setting. Locations of receivers are mapped in Fig. 6.

for deriving Dynamic Equivalent Signals) approach by Lenti & Martino (2010). The LEMA_DES procedure generates a sequence of functions and signals that (1) provide for the selection of characteristic frequencies from a smoothed Fourier spectrum of a reference accelerogram; (2) achieve a null integral over the entire duration of the final signal and a spectral density that is negligible at frequencies lower than the minimum characteristic one and (3) produce a resulting multifrequential dynamic equivalent signal that is energy-equivalent to the reference signal, best-fitted in terms of the PGA via an iterative procedure performed on the number of equivalent cycles and whose time duration is significantly shorter than that of the reference signal. The use of this approach in dynamic numerical modelling guarantees (Lenti & Martino 2010) (i) checking that the frequency content of the derived signals is defined within a representative/admissible range; (ii) avoiding exceeding the upper-threshold frequency in the modelling; (iii) narrowing the energy gap between the real and simulated seismic actions; (iv) controlling the maximum intensity of the adopted action and (v) reducing the computational time (especially in the case of parametric analyses, where a high number of iterations are requested), as the equivalent input is typically shortened with respect to the reference.

Following the CPB approach, the obtained results were plotted on graphs showing the computed *x*-disp for each applied input, corresponding to the characteristic ratios T_s/T_m and T_l/T_m. These distributions allow discussing the roles of both the 1-D resonance and the 2-D input-slope interaction in the induced displacements, as they are related to the T_s/T_m and T_l/T_m, respectively.

DISCUSSION

The results obtained from the LMM analysis for the Güevejar and Diezma landslides highlight significant differences in the earthquake-induced effects on the landslide mass.

In the case of the Güevejar landslide (Fig. 15), for each AI value, the maximum displacements are achieved for a T_l/T_m ratio lower than 2 and a T_s/T_m ratio lower than 0.5. According to the theory, this means that the role of the 2-D interactions between the landslide mass and seismic waves is more relevant with respect to the landslide 1-D resonance. Such a finding is in agreement with (i) the historical reactivations of the landslide, which occurred for high-magnitude far earthquakes and not for middle-magnitude nearby earthquakes; (ii) the HVSRs from noise and earthquake records that reveal that no 1-D resonance exists in the landslide mass and (iii) the results of the 2-D numerical modelling and of the SSRs from earthquakes that reveal a moderate local seismic amplification.

The maximum expected displacements for the Güevejar landslide are in the range of 1–10 cm for the considered range of AI values. These values seem reliable if compared with data reported by Sanz (1997) and referred to the 1755 Lisbon earthquake, as the observed crack opening due to the landslide reactivation was almost 50 cm 1 d after the main shock and reached almost 3 m after 10 d. Such a delayed displacement can be referred to the post-seismic inertial and creep movement of the landslide mass (Ambraseys & Srbulov 1995), while the co-seismic displacement of the landslide should be lower than 50 cm.

With respect to uncertainties about the historical movements of the Güevejar landslide, historical data do not inform about possible changes in the groundwater level or in the discharge of springs in the area of the landslide. In contrast, they are clearly described at other sites, especially in the epicentral area. This leads to the supposition that no significant changes could occur, so its possible effect on the stability of the slope may be ignored. Furthermore, even if the movement of the Güevejar landslide is well documented for both the 1755 Lisbon and 1884 Andalusia earthquakes, the historical occurrence itself introduces uncertainties about the real location of the hypo/epicentres; nevertheless, in both cases, the approximate location of the epicentral areas may be outlined from historical data. In the case of the 1755 Lisbon earthquake, given the well-documented tsunami triggered in the Atlantic Ocean and the great damage produced in S Portugal, several authors proposed that its source should be located S of Portugal, in the Atlantic Ocean (Martínez Solares 2001; Barkan *et al.* 2009). As a consequence, the epicentral distance to the landslide is several hundreds of kilometres, and there is no doubt that the landslide occurred very far from the epicentral area with respect to the available upper-bound curves (Rodriguez *et al.* 1999). In the case of the 1884 Andalusia earthquake, there were several scientific groups of different nationalities (Spanish, French and Italian commissions) that visited the zone immediately after the earthquake and compiled data on damage and ground effects. Several historical reports (Fernández de Castro *et al.* 1885; Taramelli & Mercalli 1886; among others) describe where large ground failures are, delineating a zone approximately 20 km long that has been interpreted as a coseismic surface rupture (Muñoz & Udías 1980). Historical data for the 1884 Andalusia earthquake are therefore abundant and allowed the creation of a detailed isoseismal map (http://www.ign.es/ign/resources/sismologia/NERIES/query_eq/index.htm) that

Table 4. Physical properties of the inputs selected for the LMM numerical modelling of the Güevejar and Diezma landslides. The properties of the LEMA_DES derived signals are identified by the postscript eq, and the per cent PGA errors with respect to the reference natural record are also reported.

	Earthquake							LEMA_DES SIGNAL					GUEVEJAR					DIEZMA			
Location	Date (yyyy/mm/dd)	Epicentral distance (km)	Mw	PGA ($m\,s^{-2}$)	Arias ($m\,s^{-1}$)	T_m (s)	n.cicles	T_{m_eq} (s)	Duration (s)	Arias_eq ($m\,s^{-1}$)	PGA_eq ($m\,s^{-2}$)	PGA error (%)	T_l (s)	T_s (s)	T_l/T_m	T_s/T_m	T_l (s)	T_s (s)	T_l/T_m	T_s/T_m
Tohoku (Japan)	2011/03/11	9700	8.9	4.40E-01	1.88E-01	16.50	/	16.50	41.01	1.88E-01	4.40E-01	/	2.60	0.50	0.16	0.03	/	/	/	/
Alpi Apunane (Italy)	2013/06/21	300	5.2	4.00E-01	1.26E-01	7.37	/	7.37	41.15	1.26E-01	4.00E-01	/	2.60	0.50	0.35	0.07	/	/	/	/
Serbia	2010/11/03	640	5.4	5.54E-01	1.65E-01	4.02	/	4.02	48.00	1.65E-01	5.54E-01	/	2.60	0.50	0.65	0.12	1.33	0.20	0.33	0.05
Montenegro	1979/04/15	21	7.0	2.11E+00	7.27E-01	0.73	2	1.430	2.80	1.50E-01	1.65E+00	19.17	2.60	0.50	3.57	0.69	1.33	0.20	1.82	0.27
Duzce (Turkey)	1999/11/12	11	7.2	7.29E-01	6.17E-02	0.16	7	1.390	10.13	1.51E-02	2.00E-01	12.33	/	/	/	/	1.33	0.20	8.31	1.25
Friuli (Italy)	1976/09/11	9	5.6	2.26E+00	2.74E-01	0.64	3	0.668	1.94	1.55E-01	1.42E+00	18.46	2.60	0.50	4.08	0.78	1.33	0.20	2.09	0.31
Izmit (Turkey)	1999/08/17	9	7.6	1.58E+00	7.05E-01	0.56	2	1.090	2.26	1.22E-01	1.72E+00	18.71	2.60	0.50	4.64	0.89	/	/	/	/
Umbria Marche (Italy)	1997/09/26	3	5.7	3.37E+00	7.01E-01	0.50	2	0.839	1.69	1.86E-01	1.86E+00	37.78	2.60	0.50	5.16	0.99	1.33	0.20	2.64	0.40
Umbria Marche (Italy)	1998/04/03	21	5.2	2.63E-01	1.18E-02	0.19	2	1.270	2.55	1.25E-03	1.47E-01	25.46	2.60	0.50	13.68	2.63	1.33	0.20	7.00	1.05
South Iceland	2000/06/21	11	6.5	4.35E+00	1.15E+00	0.38	2	2.010	4.53	1.20E-01	9.24E-01	62.14	2.60	0.50	6.79	1.31	1.33	0.20	3.47	0.52
Friuli (Italy)	1976/09/11	15	5.6	2.31E+00	3.67E-01	0.34	6	0.341	2.04	1.83E-01	1.39E+00	15.73	2.60	0.50	7.62	1.47	1.33	0.20	3.90	0.59
Friuli (Italy)	1976/05/11	4	5.0	3.02E+00	3.71E-01	0.30	2	0.453	0.89	1.11E-01	2.11E+00	1.24	2.60	0.50	8.58	1.65	1.33	0.20	4.39	0.66
Umbria (Italy)	1984/04/29	27	5.7	1.80E+00	1.36E-01	0.16	1	0.330	0.77	7.59E-02	2.63E+00	155.83	/	/	/	/	1.33	0.20	8.31	1.25
Umbria Marche (Italy)	1997/10/16	1	4.4	3.35E+00	2.04E-01	0.08	2	0.601	1.04	2.33E-02	9.26E-01	14.19	/	/	/	/	1.33	0.20	16.63	2.50
Kozani (Greece)	1995/05/13	17	6.6	7.66E-01	6.50E-02	0.20	1	0.449	0.54	1.24E-02	7.89E-01	75.66	2.60	0.50	13.00	2.50	1.33	0.20	6.65	1.00

allows locating the epicentral area at the SW border of the Granada basin, approximately 40–50 km from the Güevejar landslide. More recently, active tectonic studies done in the zone show that the co-seismic displacement associated with the Ventas de Zafarraya Fault (VZF) is the causative fault of the 1884 earthquake (Reichert *et al.* 2003).

In the case of the Diezma landslide, at the lowest AI values the maximum earthquake-induced displacements result for T_m close to the landslide mass resonance period (i.e. to a T_s/T_m ratio almost equal to 1, Fig. 16). This result is in agreement with ii) the $HVSR_s$ from noise and earthquake records, the SSR_s from earthquakes and the 2-D numerical modelling that reveal a significant seismic amplification related to the resonance of the landslide mass.

On the other hand, for increasing AI (up to 1 $m\,s^{-1}$) the maximum computed displacements result for long period signals, that is whose T_m is almost equal to $2T_l$. This is consitent with the fact that, the higher the AI is, the more relevant is the role of 2-D interactions between landslide mass and seismic waves. This result should indicate that in case of strong motion the Diezma landslide could be displaced more intensely by long period earthquakes, that is with T_m significantly lower than the landslide T_s.

As demonstrated in the theoretical study done by Lenti & Martino (2013), at low T_s/T_m ratios and at high AI values (i.e. greater than 1 $m\,s^{-1}$), the traditional sliding block methods (following Newmark's approach), which do not account for the bi-dimensional propagation of seismic waves, predict earthquake-induced displacements lower than those predicted by the dynamic numerical models.

Compared with the theoretical results for a rototranslational landslide occurring on a 15° dipping slope under linear conditions (Lenti & Martino 2013) the *x*-disp computed for the Diezma landslide are generally in very good agreement with the expected values (Fig. 16). On the other hand, in the case of the Güevejar landslide (Fig. 15) the theoretical solutions overestimate the expected *x*-disp at the highest AI ($\geq$0.1 $m\,s^{-1}$); this can be related to the lower dip of the slope as well as to the non-linearity related to the decay curves reported in Fig. 10, which occurs at lower shear strain levels than for the Diezma landslide.

In the graphs of Figs 15 and 16, the displacement values from the traditional sliding block methods correspond to $T_s/T_m = T_l/T_m = 0$, as they were obtained according to literature corelations (Lenti & Martino 2013 and references therein) existing among the critical pseudostatic coefficient of the landslide, the PGA and/or the AI value of the input, that is independent of its spectral content. These differences are justified because the traditional approaches cannot consider the increasing displacements at low T_l/T_m ratios, that is related to seismic wave propagation within the landslide mass with a predominant half-period very close to the length of the landslide mass.

It is notable that in the case of Güevejar landslide, the Newmark's displacements are negligible for all the considered AI values of the inputs; on the other hand, in the case of the Diezma landslide, the Newmark's displacements increase from less than 0.001 m up to 0.03 m with the increasing AI of the inputs.

The relevance of this study consists of the experimental work performed by considering two actual (not theoretical) landslides that are very different with respect to the involved volumes, dimensions, material properties and expected triggering conditions. The differences observed in the two case studies, in terms of both the surveyed experimental data and numerical modelling results, may be strictly related to the geometric and mechanical variables of the problem. More generally, these findings show that

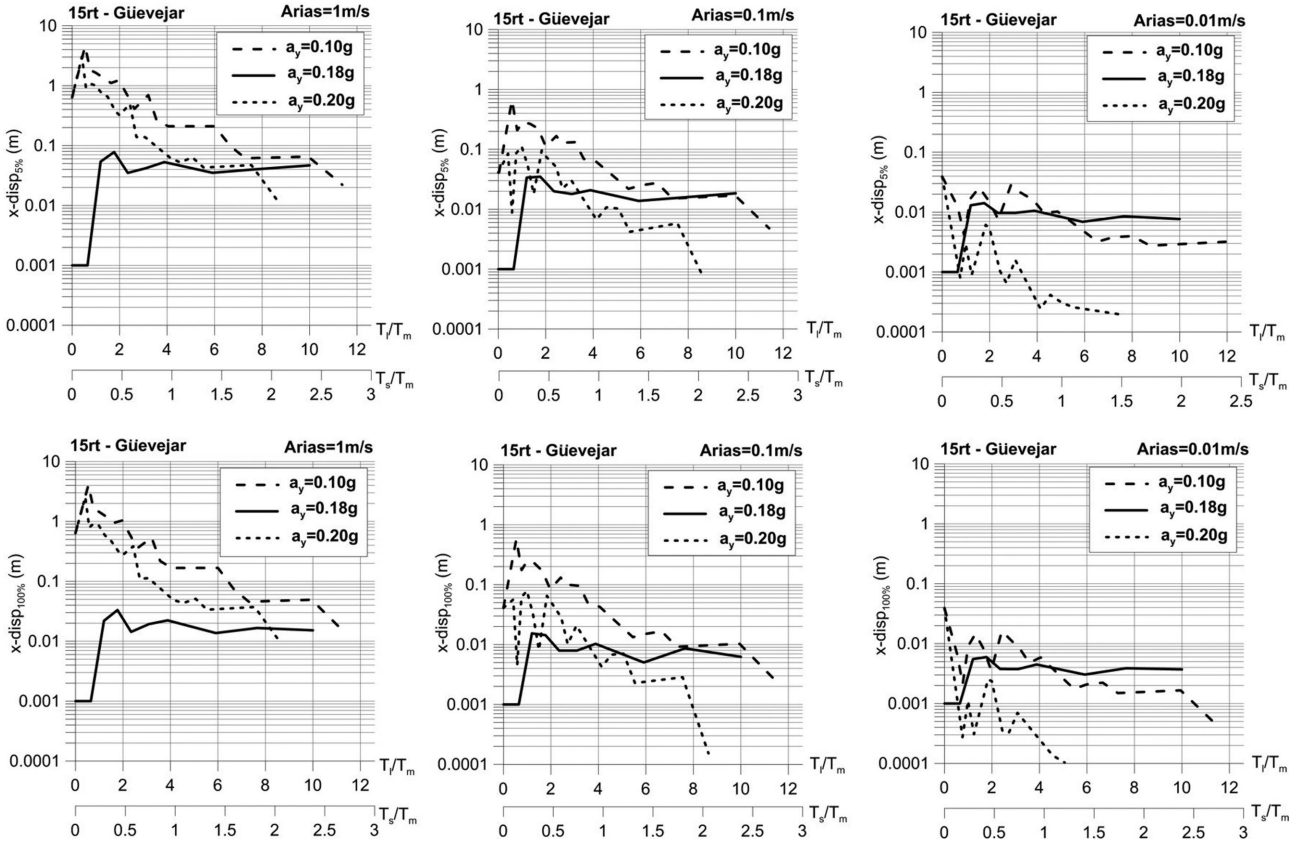

Figure 15. *x*-disp versus T_l/T_m and T_s/T_m characteristic ratios obtained for the Güevejar landslide (solid black line) by considering AI values varying from 0.01 up to 1 m s^{-1}. Only results referred to 5 per cent (upper row) and 100 per cent (lower row) of the landslide mass are here reported. The theoretical values from Lenti & Martino (2013) are also plotted (dashed lines), referred to a 15° dipping slope and a rototranslational landslide mechanism.

deterministic approaches are suitable if high-resolution provisions in terms of expected earthquake-induced displacements are requested. Such a consideration is particularly relevant because the displacements computed by the conventional sliding block methods do not necessarily overestimate the expected landslide movements respect to the CPB approach presented here.

CONCLUSIONS

This study proposes an application of a CPB approach to evaluate the earthquake-induced displacements of landslides by stress–strain dynamic numerical modelling, that is not assuming a rigid sliding block condition. This approach consists of computing the displacements cumulated within the landslide mass and relating them to the ratios between the characteristic periods of the landslide masses (T_s and T_l), related to their thickness and length, respectively, and that (T_m) of the seismic signal. Two landslides located in southern Spain were considered: the Güevejar landslide, which is approximately 1 km length, was re-activated by historical earthquakes and exemplifies a very large unstable mass that can interact with long to very long period seismic waves (i.e. >2.6 s). The Diezma landslide is approximately 400 m length, was man-induced and has not yet been re-activated by earthquakes; it exemplifies a large landslide that can interact with shorter-period waves (i.e. >1.3 s). Depending on the landslide mass thickness, the Güevejar landslide is characterized by a resonance period close to 0.5 s, while the Diezma landslide is characterized by a 0.2 s resonance period. According to the numerical modelling outputs, for the Güevejar landslide, the maximum displacements are expected for inputs having a T_l/T_m ratio very close to the theoretical value of 0.5 for each AI level, while no relevant effects are related to inputs with a theoretical value of T_s/T_m close to 1. This is confirmed by the negligible amplification due to the landslide mass resonance that was recorded by *in situ* geophysical investigations. On the other hand, for the Diezma landslide, maximum displacements are expected for inputs having a T_l/T_m ratio very close to the theoretical value of 0.5 at the highest AI level (on the order of 1 m s^{-1}) and for inputs having a T_s/T_m ratio very close to the theoretical value of 1 for the lower AI levels (on the order of 0.1–0.01 m s^{-1}). Such a result is in very good agreement with the geophysical evidence of a high amplification existing within the landslide mass and related to its resonance.

The comparison between the two landslide case studies demonstrates the relevance of the role of length in the case of km-scale landslides in terms of the effects expected by the interaction with seismic waves, while, on the other hand, the landslide mass resonance, mainly related to its thickness, plays a more significant role in the case of hm-scale landslides. In both the considered case studies, the more conventional Newmark's approach significantly underestimates the earthquake-induced displacements, even if flexible bock conditions are taken into account.

These findings encourage the use of a CPB approach, particularly for the deterministic analysis of earthquake-induced displacements, that is in the case of a single landslide study. On the other hand, such an analytical approach is less suitable in the case of more extensive analyses of earthquake-induced landslide displacements (i.e. referring to numerous events inventoried in a wide region), as

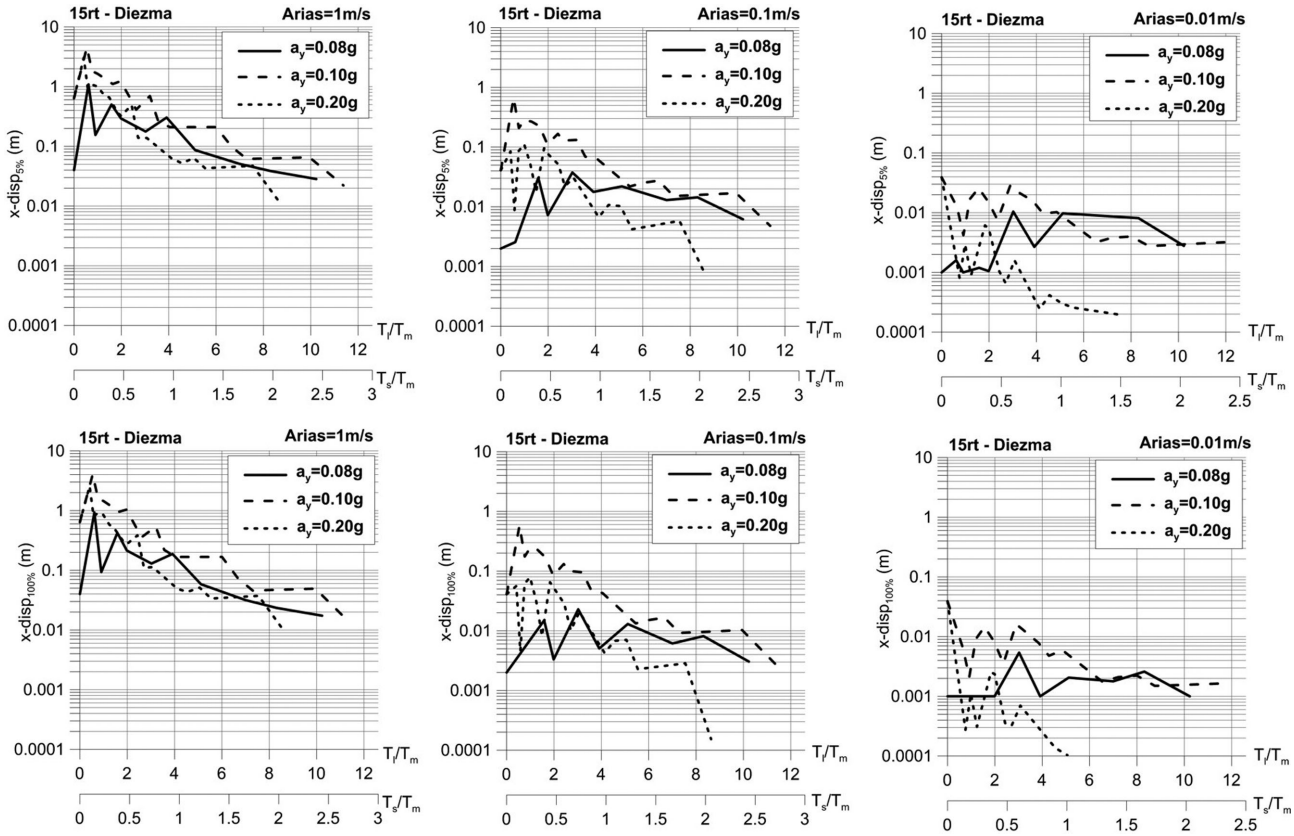

Figure 16. *x*-disp versus T_l/T_m and T_s/T_m characteristic ratios obtained for the Diezma landslide (solid black line) by considering AI values varying from 0.01 up to 1 m s^{-1}. Only results referred to 5 per cent (upper row) and 100 per cent (lower row) of the landslide mass are here reported. The theoretical values from Lenti & Martino (2013) are also plotted (dashed lines), referred to a 15° dipping slope and a rototranslational landslide mechanism.

several numerical solutions are necessary due to the use of different seismic inputs (i.e. by characteristic ratios, T_l/T_m and T_s/T_m, varying over a suitable range). Based on these reported results, the landslide dimensions should be taken into account to guarantee a more conservative approach for computing the earthquake-induced expected displacements, that is to select inputs with the most critical characteristic periods.

ACKNOWLEDGEMENTS

The authors would like to thank the European Union ERDF for financial support via the 'Monitorización sísmica de deslizamientos. Criterios de reactivación y alerta temprana' project of the 'Programa Operativo FEDER de Andalucia 2007–2013'. We would also like to thank the staff and researchers at the Agency of Public Works and Regional Ministry of Public Works and Housing of the Andalusia Regional Government for their dedication and professionalism.

The Authors wish to thank Alessandra Noviello, Manuela Palmas, Fabiola Tammaro and Ester Villaplana for their contribution to field activities and data processing. Luigi Stedile and Jean Louis Tacita for the technical support in the laboratory tests. The authors also thank H.B. Havenith and another anonymous reviewer for the useful suggestions provided to improve this paper.

REFERENCES

Alfaro, P., Delgado, J., Garcia-Tortosa, F.J., Giner, J.J., Lenti, L., Lopez-Casado, C., Martino, S. & Scarascia Mugnozza, G., 2012. The role of near-field interaction between seismic waves and slope on the triggering of a rockslide at Lorca (SE Spain), *Nat. Hazards Earth Syst. Sci.*, **12,** 3631–3643.

Ambraseys, N. & Srbulov, M., 1995. Earthquake induced displacements of slopes, *Soil Dyn. Earthq. Eng.,* **14,** 59–71.

ASTM D4015-92, 2000. Standard Test Methods for Modulus and Damping of Soils by the Resonant-Column Method, ASTM International, West Conshohocken, PA, 2000, www.astm.org.

ASTM D4767-04, 2000. Standard Test Method for Consolidated Undrained Triaxial Compression Test for Cohesive Soil. ASTM International, West Conshohocken, PA, 2000, www.astm.org.

Azañón, J.M. *et al.*, 2010. Regional-scale high plasticity clay-bearing formation as controlling factor on landslides in Southeast Spain, *Geomorphology*, **120,** 26–37.

Barkan, R., ten Brink, U.S. & Lin, J., 2009. Far field tsunami simulations of the 1755 Lisbon earthquake: implications for tsunami hazard to the U.S. East Coast and the Caribbean, *Mar. Geol.*, **264,** 109–122.

Borcherdt, R.D., 1994. Estimantes of site-dependent response spectra for design (methodology and justification), *Earthq. Spectra*, **10,** 617–653.

Bouckovalas, G.D. & Papadimitriou, A.G., 2005. Numerical evaluation of slope topography effects on seismic ground motion, *Soil Dyn. Earthq. Eng.*, **25,** 547–558.

Bourdeau, C. & Havenith, H.B., 2008. Site effects modeling applied to the slope affected by the Suusamyr earthquake (Kyrgyzstan, 1992), *Eng. Geol.*, **97,** 126–145.

Bozzano, F., Lenti, L., Martino, S., Paciello, A. & Scarascia Mugnozza, G., 2008. Self-excitation process due to local seismic amplification responsible for the reactivation of the Salcito landslide (Italy) on 31 October 2002, *J. geophys. Res.*, **113,** B10312, doi:10.1029/2007JB005309.

Bozzano, F., Lenti, L., Martino, S., Paciello, A. & Scarascia Mugnozza, G., 2011. Evidences of landslide earthquake triggering due to self-excitation process, *Int. J. Earth Sci.*, **100,** 861–879.

Cetin, K.O., Isik, N. & Unutmaz, B., 2004. Seismically induced landslide at Degirmendere Nose, Izmit Bay during Kocaeli (Izmit)-Turkey earthquake, *Soil Dyn. Earthq. Eng.*, **24,** 189–197.

Cruden, D.M & Varnes, D.J., 1996. Landslide types and processes, in *Landslides: investigation and mitigation. Transportation Research Board*, pp. 36–75, Spec. Report 247, eds Turner, A.K. & Schuster, R.L., National Research Council, National Academy Press, Washington, DC.

Cundall, P., Hansteen, E., Lacasse, S. & Selnes, P.B., 1980. NESSI, soil structure interaction program for dynamic and static problems, Norges Geotekniske Institute, Norway, Report 51508-9.

Danneels, G., Bourdeau, C., Torgoev, I. & Havenith, H.B., 2008. Geophysical investigation and dynamic modeling of unstable slopes: case-study of Kainama (Kyrgyzstan), *Geophys. J. Int.*, **175**(1), 17–34.

Del Gaudio, V. & Wasowski, J., 2007. Directivity of slope dynamic response to seismic shaking, *Geophys. Res. Lett*, **34,** L12301, doi:10.1029/2007GL029842.

Delgado, J., Garrido, J., López-Casado, C., Martino, S. & Peláez, J.A., 2011. On far field occurrence of seismically induced landslides, *Eng. Geol.*, **123,** 204–213.

Delgado, J., Garrido, J., Lenti, L., Lopez-Casado, C., Martino, S. & Sierra, F.J., 2015. Unconventional pseudostatic stability analysis of the Diezma landslide (Granada, Spain) based on a high-resolution engineering-geological model, *Eng. Geol.*, **184,** 81–95.

Fernández Castro, M., Lasala, J.P., Cortázar, D. & Gonzalo y Tarín., J., 1885. Terremoto de Andalucía: Informe de la Comisión nombrada para su estudio dando cuenta del estado de los trabajos en 7 de marzo de 1985, *Boletín de la Comisión del Mapa Geológico de España*, **T. XII,** 1–105.

Field, E.H. & Jacob, K., 1995. A comparison and test of various site response estimation techniques, including three that are non reference-site dependent, *Bull. seism. Soc. Am.*, **85,** 1127–1143.

Hutchinson, J.N., 1994. Some aspects of the morphological and geotechnical parameters of landslides, with examples drawn from Italy and elsewhere, *Geol. Romana*, **30,** 1–14.

IGME, 1988. Mapa geológico de España, E: 1:50.000, Hoja Núm. **1009** (Granada), Madrid.

ITASCA, 2011. FLAC 7.0: User manual, Licence number 213-039-0127-18973, Earth Science Department, Sapienza-University of Rome.

Jiménez Pintor, J.J. & Azor, A., 2006. The Güevéjar landslide: a case study of slope instability triggered by earthquakes, *Geogaceta*, **40,** 287–290.

Keefer, D.K., 1984. Landslides caused by earthquakes, *Geol. Soc. Am. Bull.*, **95,** 406–421.

Kuhlemeyer, R.L. & Lysmer, J., 1973. Finite element method accuracy for wave propagation problems, *J. Soil Mech. Found, Div. ASCE*, **99**(SM5), 421–427.

Lenti, L. & Martino, S., 2010. New procedure for deriving multifrequential dynamic equivalent signals (LEMA_DES): a test-study based on Italian accelerometric records, *Bull. Earthq. Eng.*, **8,** 813–846.

Lenti, L. & Martino, S., 2012. The interaction of seismic waves with step-like slopes and its influence on landslide movements, *Eng. Geol.*, **126,** 19–36.

Lenti, L. & Martino, S., 2013. A parametric numerical study of the interaction between seismic waves and landslides for the evaluation of the susceptibility to seismically induced displacements, *Bull. seism. Soc. Am.*, **103,** 33–56.

Makdisi, F.I. & Seed, H.B., 1978. Simplified procedure for estimating dam and embankment earthquake-induced deformations, *J. Geotech. Engrg. Div., ASCE*, **104**(7), 849–867.

Martínez Solares, J.M., 2001. The great historical 1755 earthquake. Effects and damage in Spain, *J. Seismol.*, **8,** 275–294.

Martínez Solares, J.M., Cabañas, L., Benito, B., Ricas, A., Gaspar, J.M., Ruíz, S. & Rodríguez, O., 2013. *Actualización de mapas de peligrosidad sísmica de España 2012*. Gobierno de España, Ministerio de Fomento, 267 pp.

Martino, S., 2015. Earthquake-induced reactivation of landslides: recent advances and future perspectives, in *Earthquakes and Their Impact on Society,* pp. 291–322, ed. D'Amico, S., Springer International Publishing.

Meléndez, B. & Fuster, J.M., 1966. *Geología,* Paraninfo.

Muñoz, M. & Udías, A., 1980. Estudio de los Parámetros y Serie de Réplicas del Terremoto de Andalucía del 25 de Diciembre de 1884 y de la Sismicidad de la Región Málaga-Granada, Instituto Geográfico Nacional, El Terremoto de Andalucía de 1884, Madrid, pp. 95–139.

Nakamura, Y., 1989. A method for dynamic characteristics estimations of subsurface using 683 microtremors on the ground surface, *Quart. Rept. RTRI Japan*, **30,** 25–33.

Newmark, N.M., 1965. Effects of earthquakes on dams and embankments, *Geotechnique*, **15**(2), 139–159.

Otter, J.R.H., Cassell, A.C. & Hobbs, R.E., 1966. Dynamic Relaxation (Paper No. 6986), *Proc. Inst. Civil Eng.*, **35,** 633–656.

Rathje, E.M. & Bray, J.D., 2000. Nonlinear coupled seismic sliding analysis of earth structures, *J. Geotech. Geoenviron. Eng., ASCE*, **126**(11), 1002–1014.

Rathje, E.M., Abrahamson, N.A. & Bray, J.D., 1998. Simplified frequency content estimates of earthquake ground motions, *J. Geotech. Geoenvir. Eng., ASCE*, **124**(2), 150–159.

Reicherter, K.R., Jabaloy, A., Galindo-Zaldívar, J., Ruano, P., Becker-Heidmann, P., Morales, J., Reiss, S. & González-Lodeiro, F., 2003. Repeated palaeoseismic activity of the Ventas de Zafarraya fault (S Spain) and its relation with the 1884 Andalusian earthquake, *Int. J. Earth Sci. (Geol Rundsch)*, **92,** 912–922.

Rodriguez, C.E., Bommer, J.J. & Chandler, R.J., 1999. Earthquake-induced landslides: 1980–1997, *Soil Dyn. Earthq. Eng.*, **18,** 325–346.

Rodríguez-Peces, M.J., Azañón, J.M., García-Mayordomo, J., Yesares, J., Troncoso, E. & Tsige, M., 2011. The Diezma landslide (A-92 motorway, Southern Spain): history and potential for future reactivation, *Bull. Eng. Geol. Environ.*, **70,** 681–689.

Sanz, E., 1997. Le mouvement de versant de Güevéjar (Grenade) au cours des tremblements de terre de Lisbonne (1755) et d'Andalousie (1884), *Bull. Intl. Assoc. Eng. Geol.,* **56,** 83–87.

Semblat, J.F. & Pecker, A., 2009. *Waves and Vibrations in Soils: Earthquake, Traffic, Shocks, Construction Works*, IUSS Press, pp. 499.

Semblat, J.F., Dangla, P., Kham, M. & Duval, A.M., 2002a. Seismic site effects for shallow and deep alluvial basins: in-depth motion and focusing effect, *Soil Dyn. Earthq. Eng.*, **22**(9), 849–854.

Semblat, J.F., Duval, A.M. & Dangla, P., 2002b. Seismic site effects in a deep alluvial basin: numerical analysis by the boundary element method, *Comput. Geotech.*, **29**(7), 573–585.

SESAME Working Group, 2004. Guidelines for the implementation of the h/v spectral ratio technique on ambient vibration measurements, processing and interpretation, Available at: http://sesame-fp5.obs.ujf-grenoble.fr/Delivrables/Del-D23-HV_User_Guidelines.pdf, last accessed February 2015.

Taramelli, T. & Mercalli, G., 1886. I terremoti andalusi cominciati il 25 Dicembre 1884, *Reale Accademia dei Lincei - Memorie della Classe di Science Fisiche, Matematiche e Naturali*, **3**(4), 116–222.

Wathelet, M., Orhnberger, M., Köhler, A. & Cornou, C., 2011. Geophysical signal database for noise array processing (GEOPSY – release 2.7.4), Available at: http://www.geopsy.org/download.php, last accessed February 2015.

Wilkins, M.L., 1964. Fundamental methods in hydrodynamics, in *Methods in Computational Physics*, Vol. 3, pp. 211–263, eds Alder *et al.*, Academic Press.

WP/WLI (International Geotechnical Societies' UNESCO Working Party for World Landslide Inventory), 1993. A suggested method for describing the activity of a landslide, *Bull. Int. Assoc. Eng. Geol.*, **47,** 53–57.

Zhai, E., Roth, W., Dawson, E. & Davis, C., 2004. Seismic deformation analysis of an earth dam—a comparison study between equivalent-linear and nonlinear effective-stress approaches, in *Proceedings of the 13th World Conference on Earthquake Engineering*, Vancouver, B.C., Canada, 2004 August 1–6, Paper No. 3298.

Zienkiewicz, O.P., 2005. *The Finite Element Method*, McGraw-Hill, 785pp.